

#6



Vol 42, No. 3 - High-Resolution Displays

[ Table of contents: [HTML](#), [ASCII](#) ]

Feature article

0018-8646/98/\$5.00 © 1998 IBM

## Contrast properties of reflective liquid crystal light valves in projection displays

by A. E. [Rosenbluth](#), D. B. [Dove](#), F. E. [Doany](#), R. N. [Singh](#), K. H. [Yang](#), and M. [Lu](#).

Projectors that use reflective light valves must employ beam splitters or analogous components to separate bright-state light from dark-state light, since both states must propagate in the space above the light valve. Polarization ray tracing shows that such beam splitters will not usually achieve high rejection of dark-state light when the beam has the typical angular divergence of about  $\pm 10^\circ$ . At such propagation angles, different rays in the beam will have appreciably different planes of incidence at tilted optical coatings in the system (because of the compound angles involved). If the light valve is mirrorlike in dark state, we show that to correct the depolarization resulting from compound incidence angles, it is necessary that the optics introduce no rotation in the illuminating polarization. To a reasonable approximation, such a rotation in polarization will double in the return pass through the optics. To the same approximation, induced ellipticity in the illuminating polarization will cancel in double pass, and pure rotation can be converted to pure ellipticity with a quarterwave retarder. An important qualification, however, is that a light valve can only be exactly mirrorlike in restricted cases [i.e., if linearly polarized input light remains exactly linearly polarized (though possibly rotated) at all wavelengths when it reaches the mirror backplane of the light valve, independent of small manufacturing errors]. We calculate contrast loss in the more realistic case of a reflective twisted nematic liquid crystal (TNLC) light valve interacting with tilted coatings in the projection optics over finite numerical aperture (NA), and discuss the impact on LC thickness tolerances and spectral bandwidth  $\Delta\lambda$ . We extend our results to apply to more general light valves and more general projection optics configurations. Dark-state background is found

**to scale as  $NA^2$  (or in some cases as  $\sim NA^2 \Delta\lambda^2$ ). Because of this interaction, the complete system almost always shows a lower contrast than the light valve alone.**

## Introduction

Light valves that are reflective provide important advantages in projection displays. Controlling circuitry placed below the mirror surface does not obstruct the clear aperture [1, 2], more advanced IC technology is available for substrate materials that are opaque, and a more compact system may be achieved when the reflected output beam is folded back on the input. However, complexities arise in the optical system when the space above the light valve must be used for both illumination and collection. The reversibility of a nominally loss-free optical system implies that the light valve must be illuminated with dark-state light, because light that remains in the input state after reflecting from the light valve necessarily follows the reverse path back to the illuminator, and so does not contribute to image brightness. In different technologies the term *dark-state* might refer either to the polarization or to the directionality of the incident light, depending on the method of modulation used. In either case, it is a basic physical requirement that any light which the light valve might reflect without modification (in polarization or direction) will necessarily retrace its path back to the source.

Conversely light that is switched to the bright state by the light valve must be shunted into the projection optics. When light valves use polarization modulation, this is generally accomplished with a polarizing beam splitter (PBS), but the required angular range can be difficult to achieve. For one thing, it can be difficult to achieve acceptable performance from the polarizing hypotenuse coating over an adequate angular range (e.g., over a range of angles of incidence  $\sim 45^\circ \pm 5^\circ$  in glass).

There is, however, a more subtle problem, relating to the difficulty in maintaining a consistent polarization in a three-dimensional cone of light as it propagates through an optical system. The angular subtense required in the beam [essentially, the numerical aperture (NA) or  $f/\#$ ] is dictated by the need for high lumen output, often the paramount requirement in today's projection displays. Typical output requirements and efficiency constraints imply optical fluxes at the light valve of  $\sim 1$  W. Integrated-circuit processing techniques typically constrain the aperture of reflective light valves to dimensions of a few centimeters or less. Brightness limits in today's short-arc lamps then imply that the beam illuminating the light valve must subtend at least several degrees in order to provide the necessary flux density [3]. Polarization control with twisted nematic liquid crystal (TNLC) light valves and PBS optics over such angular ranges are the main emphasis of this paper. However, it is worth noting that the problem of preventing "crosstalk" between bright-state and dark-state beams is fairly general with reflective light valves, affecting, for example,

those based on directional modulation.

Broadband polarizing beam splitters have been procured commercially<sup>1</sup> that provide dark-state rejection  $>250:1$  throughout the visible spectrum if used single-pass at any angle within a  $\pm 10^\circ$  range. (A supplementary sheet polarizer must be included when the PBS is used in reflection.) **Figures 1 and 2** illustrate the coating performance achieved. Imperfect coating response was distinguished from substrate birefringence in the measurements in **Figures 1 and 2** by crossing the PBS pass direction against parallel input and output sheet polarizers. Measurements with a solid cube were used to subtract out losses in the prism substrates and front-surface antireflection coatings. Some PBS substrate glasses introduce appreciable attenuation in the blue region of the spectrum, but blue losses in the substrates of **Figures 1 and 2** were small compared to those arising in other parts of the system, e.g. from illuminator components and aluminum fold mirrors [3]. The plotted results are integrated over a uniform cone of rays at each NA. It should be noted that while this coating provides reasonably high efficiency out to  $NA \sim 0.2$ , the design range was only  $\pm 6^\circ$ .

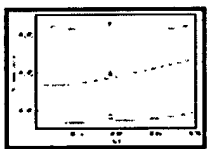


Figure 1

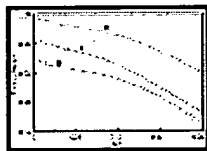


Figure 2

In a projector the PBS must be used in both transmission and reflection. One mode (e.g., transmission) is used for the illumination pass to the light valve, and the other (e.g., reflection) for collection from the light valve by the projection lens. MacNeille-type PBS coatings are designed to be dielectric mirrors in S polarization; a far more difficult requirement in their design is that they achieve Brewster suppression of  $P$  reflectivity throughout the  $\sim \pm 10^\circ$  angular range. In practice, achieved  $P$  transmittance always departs much further from the goal of 100% than does S reflectance, so  $P$  transmittance gates double-pass PBS efficiency. Total background light in projection displays must typically be  $\lesssim 1$  part in 100 of bright state; the departure of  $P$  transmittance from unity is inevitably larger than this, which means that a supplementary polarizer (e.g., a sheet polarizer) must be included in the reflection pass to block reflected  $P$  light (i.e., if the light valve is illuminated with light reflected from the PBS hypotenuse, the illumination must be passed through a sheet polarizer before entering the PBS; if instead the image light is collected in reflection, the image light must be passed through a sheet polarizer after reflecting from the PBS). Sheet polarizers are at best  $\sim 90\%$  efficient in the pass polarization, and it is desirable that the S transmittance be low enough that one does not have to add a second lossy sheet polarizer for the transmission arm. (Note that such a sheet polarizer in the illuminator might be replaced by more expensive polarizing elements that partially recycle the unused polarization [3-5].) **Figures**

1 and 2 show that coatings available today can achieve these performance goals; single-pass reflectance of *P* polarization and single-pass transmission of *S* polarization are both acceptably low by the above criteria.

However, basic trigonometric constraints limit the rejection ratio that can be achieved by the PBS element in double-pass, if it is used to illuminate a reflective substrate with a noncollimated beam. If the light valve returns dark-state light in mirrorlike fashion, the geometry of compound angles implies that skew rays will not see the same plane of incidence at the return pass to the PBS hypotenuse that they see on the input pass.

For skew rays these planes of incidence are tilted relative to the external faces of the PBS cube. For example, **Figure 3** shows a skew ray AB incident at the front face of a PBS cube; the ray illuminates the light valve at point C after being reflected downward from point B by the hypotenuse coating. If the light valve is switched dark, the ray remains (nominally) dark-state polarized, and returns to the front face along CB'A'. During the input pass the PBS will polarize the illumination either perpendicular to the tilted plane of incidence ABC (for illumination in reflection through the PBS, as shown in Figure 3), or within this tilted incidence plane (for illumination in transmission, not shown in Figure 3). If the illumination polarization is maintained in the dark-state light that reflects from the light valve, the *E*-field will show a different tilt relative to the new plane of incidence for the return pass at the PBS hypotenuse (plane A'B'C). The top-view diagram of Figure 3 illustrates the incident and returned *E*-field for the case of a light valve with mirrorlike dark state. The returned skew ray is reflected to the opposite side of the lens NA, causing the return plane of incidence A'B'C to have an opposite tilt from the input incidence plane ABC. The newly tilted orientation of the *E*-field relative to A'B'C means that the dark-state light has both *S* and *P* components during the return pass, and so is not entirely returned to the illuminator.

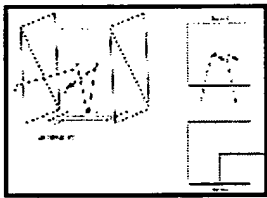


Figure 3

By this mechanism, the compounded incidence angle of the ray at the PBS coating (the ray incidence angle having components along both the skew and coating-tilt meridians) gives rise to polarization crosstalk, causing a loss in contrast. The amplitude projection onto the tilted incidence plane is approximately linear with NA, and contrast decreases as  $NA^{-2}$ . Since compound-angle depolarization converts dark-state light to the bright state of the image, this NA-dependent background cannot be filtered out with a supplementary polarizer.

This depolarization mechanism does not ordinarily arise with transmissive light valves, where a simple sheet post-polarizer can be used to trim dark-state light from the bright-state image beam. When the light valve is reflective, both states must propagate in the space above the substrate, and the beam-splitter element must actually separate the two beams. Beam-dividing interference coatings are prone to the depolarization mechanism described above. A transmission light valve will not suffer compound-angle depolarization even when PBS pre- and post-polarizers are used instead of sheet polarizers, as long as the hypotenuse coatings of the two PBS cubes are parallel and there are no other tilted coatings between the PBSs and the light valve. However, single-pass compound-angle effects are reported [6] in rear-projection monitors that reduce box depth by using a reflective polarizer [7, 8] on the inside surface of the projection screen in order to make an extra fold in the imaging beam [6, 9].

As discussed above, the ideal reflective light valve must, when switched to dark-state, reflect the central ray without changing its polarization. However, such an ideal light valve need not be mirrorlike; it might, for example, be instead equivalent to a quarter-wave retarder placed above a mirror. As long as the fast and slow axes of such a retarder take the orientation shown by the dashed lines in Figure 3 (one axis lying within the plane BB'C, the other axis parallel to the central ray before it enters the cube), the dark-state polarization of the input central ray will remain unchanged in the output. However, such a quarter-wave retarder will change the polarization of skew rays, in a beneficial way. The retarder will act as a half-wave rotator in double pass, and the  $E$ -field of a skew ray that is incident perpendicular to (or within) the rotated plane ABC will be returned in a direction perpendicular to (or within) the mirror-rotated plane A'B'C, thereby eliminating depolarization [10]. If the dark-state light valve resembles a mirror rather than a quarter-wave plate, the same correction can of course be obtained by placing an actual quarter-wave retarder above the light valve. This technique appears to be fairly well known among manufacturers of light-valve projectors (perhaps having been invented independently a number of times), but to our knowledge it has only been described in the patent literature [10].

In this paper we describe the above depolarization mechanism in more general terms; we consider more general optical systems than the simple PBS of Figure 3, and we consider light valves that are not necessarily ideal. We do, however, make the following approximation: In cases where the central ray strikes a surface at (or near) normal incidence, we apply the normal-incidence Jones matrix for the surface to all rays in the beam. (In fact, it is only in this approximation that one can describe the  $E$ -field reflected from a mirror as not rotated.) Terms that scale as  $NA^2$  (in amplitude) are thereby neglected. However, we show that tilted optical coatings in the system give rise to amplitude effects that scale as  $NA^1$  (as in the example of Figure 3); these linear terms are dominant. Comparison

with exact-polarization ray tracing shows that a first-order calculation predicts background levels to well below one part in 100 at NAs of interest to us, i.e., at apertures below  $\sim f/3.5$  ( $NA \approx 0.14$ ). (When we use the term *first-order* in this work without further qualification, we mean first-order in an expansion in beam NA.) More accurate calculations require modeling of the angular dependence of near-normal incidence components such as linear sheet polarizers and the light valve; these are beyond the scope of the present paper. However, we note that the mechanics of exact-polarization ray tracing are well known in the literature, and are implemented in commercial optical design programs. Most commonly, polarization along a ray is determined from a multiplied string of Jones matrices, alternating between matrices for the surfaces and matrices that carry out rotation transforms to map the S and P polarization directions of one surface to the S and P directions for the next. To our knowledge, the first such treatment to use a modern ray-tracing formulation is that of Waluschka [11]; full implementation details are given in his paper. Waluschka's method is useful for calculating the polarization properties of projection optics at a system level. The polarization properties of LC light valves are described in two recent reviews [12, 13].

A first-order calculation is sufficiently accurate for our purposes, and the simplification it provides yields two advantages. First, such a calculation allows contrast to be defined in terms of simple relationships involving surface parameters (usually, the surface orientations and the S/P relative phase shifts from interference coatings on the surfaces). Simple relationships are particularly advantageous in an optimization program, where rapid evaluation of a merit function is important.

Second, a first-order analysis provides considerable insight into the nature of contrast loss from interaction between the optics and the light valve. This is the main emphasis of the present paper. Contrast with a general optical system and light valve is found to scale as  $NA^{-2}$  under the compound-angle depolarization mechanism. The analysis below shows that a succession of optical surfaces that are parallel to the PBS hypotenuse (in media having roughly similar refractive indices) do not give rise to further depolarization. Only surfaces where bright-state and dark-state light propagate together give rise to relevant depolarization; as illustrated in **Figure 4**, these might include color-splitting dichroics between the PBS and the light valves. Only bright-state light propagates between the PBS and the projection lens, but dark-state and bright-state light must both propagate through surfaces that lie between the PBS and the light valve, and dark-state light traverses these surfaces in double pass. This double-pass traversal implies a degree of symmetry in the depolarization properties; we show that when the dark-state light valve can be approximated as mirrorlike, rotation imposed on the illuminating polarization by the optics during the input pass is essentially doubled during the output pass, and ellipticity is canceled. This is opposite to the usual symmetry in double-pass traversal of a polarizing element, where

(for small depolarization) ellipticity doubles and rotation is canceled (as with a waveplate or optically active film above a mirror); the difference is that a skew ray propagates through the optics on opposite sides of the pupil during the input and output passes.

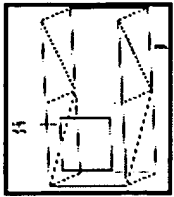


Figure 4

Note that what is meant here by "doubling of rotational depolarization in round trip" is that when the single-pass depolarization of skew rays is purely rotational (i.e.,  $E_x/E_z$  is pure real at the completion of a single pass through the optics when the input ray cone is linearly polarized along  $\hat{z}$ , with optical axis along  $\hat{y}$ ), the double-pass depolarization will be twice as large in magnitude. The double-pass intensity between crossed polarizers is then four times that measured in single pass if the single-pass depolarization is purely rotational. However, while the depolarization doubles in magnitude after two passes, the direction of polarization in the beam that exits the system is always aligned with the PBS pass axis for the bright-state image, which is oriented at approximately  $90^\circ$  to the polarization that illuminates the light valve.

It is not necessary that the light valve be mirrorlike in dark state to provide high contrast. We later show [Equation (64)] that when any continuous polarization-modulating layer is placed above a mirror backplane and rotated between crossed polarizers, the reflectance (in double-pass traversal of the layer) will be proportional to  $\sin^2(2\theta')$ , with  $\theta'$  the orientation (measured relative to the orientation of minimum reflectivity), as long as the layer is not lossy from scattering or absorption. One must imagine that the beam is incident on the reflecting structure at an angle slightly off normal, so that the input and output polarizers can be crossed to each other. The amplitude of the  $\sin^2(2\theta')$  variation is only zero (for all  $\theta'$ ) if the polarization-modulating layer (in single pass) is either null, equivalent to a half-wave retarder, or equivalent to a pure rotation (optically active layer). On the other hand, a PBS in a projector functions "in zeroth order" (i.e.,  $NA \rightarrow 0$ ) as crossed polarizers, so to zeroth order essentially any polarization-modulating film above a mirror can be said to provide a valid dark state if rotated to a particular orientation where the  $\sin^2(2\theta')$  modulation has a zero. (Of course, in practice a light-valve active layer must in dark state be reasonably insensitive to depolarization from scatter and small inhomogeneities, it must satisfy spectral bandwidth requirements, and it must provide adequate performance when  $NA \neq 0$ .)

If the light valve is not mirrorlike, we still find that when  $NA \neq 0$ , one portion of the single-pass depolarization from the optical system will be

canceled in the return pass, and the remaining portion will double (in amplitude). As noted above, depolarization refers to the complex electric field amplitude that is output with polarization in the orthogonal state to a linear polarized input, divided by the output in the parallel polarization. We show that the relationship between single-pass and double-pass contrast loss can be expressed very simply in terms of the phases of the light valve and optics depolarizations. For this reason it is convenient to analyze the projection properties of the system by propagating a single complex scalar (namely the depolarization) from surface to surface, rather than by propagating a Jones vector. However, we follow the Jones-matrix approach of Lu and Saleh [14] in analyzing the light valve.<sup>2</sup>

If a reflective light valve comprises an active polarizing layer [polarizing in the general sense of altering the polarization, e.g., a twisted nematic liquid crystal (TNLC) layer] above a bottom reflecting surface, we would expect that the conventional reversal symmetry would apply to the active layer itself. In that case, if control of the thickness of the polarizing layer is imperfect, and/or the light valve is to be used over an appreciable spectral bandwidth, we can only expect ideal contrast from the light valve in a simple crossed-polarizer measurement if the  $E$ -field within the active layer is linear at all depths close to the bottom mirror (since the exact depth of the mirror may vary), and is so linear at all wavelengths of interest. The light-valve active layer might cause the  $E$ -field at the bottom mirror to be rotated, but with the conventional reversal symmetry such rotation is canceled in the return pass through the layer. However, when the active layer produces ellipticity in the light illuminating the mirror backplane, this single-pass depolarization is not canceled in the return pass. When the single-pass depolarization is small (small rotation and small ellipticity), the elliptical component of the depolarization doubles in the return pass (in the sense that the intensity between crossed polarizers is approximately quadruple that of a transmission cell with an active layer producing the same single-pass ellipticity), causing the dark-state illumination to be partially converted to bright-state. [These results are derived below in Equation (49).] Thus, the optimum behavior for the light valve in the "zeroth-order" case where the optics is ignored is that it produce no ellipticity at any wavelength in the light illuminating the mirror backplane, despite the presence of possible variations in layer thickness. (Note that skew-angle depolarization in the optics thus obeys a symmetry opposite to that of the light valve.) Unfortunately, the absence of ellipticity at all depths and wavelengths is difficult to achieve in a medium that shows both birefringence and a twist, as with TNLC. [An exception is a TNLC operating in the Maugin limit ([16]; see also [17, 18]); this case, however, is usually not practical for reflection light valves.] Thus, it is not surprising that, as shown below, a dark-state TN light valve of given thickness typically exhibits truly mirrorlike behavior at only a single wavelength in the operating spectral range. Even at this unique wavelength, we show that polarization rotation by the optics (but not imposed ellipticity) gives rise to dark-state background  $\propto NA^2$ . At other



wavelengths, the light valve interacts with both ellipticity and rotation imposed by the optics, again with scaling  $\propto NA^2$  or  $\propto NA^2 \Delta\lambda^2$ , where  $\Delta\lambda$  is the shift away from the optimal wavelength. If the TN light valve is used between simple crossed polarizers ( $NA \rightarrow 0$ ), background is found to scale  $\propto \Delta\lambda^4$ ; such quartic contributions are also present when the light valve is used in an optical system ( $NA \neq 0$ ).

## Analysis

### *Light valve*

The Jones matrix of a dark-state TN light valve has been derived by Lu and Saleh [14]. We use their formulation and notation, except we correct for what we believe is a sign error in their result. (This is above and beyond the difference between their sign convention and the sign convention used here.) The sign error appears to have propagated into their expression from a result of Yariv and Yeh [19]; since this result is widely cited in the literature, we sketch out the derivation here. Matrix element signs would not usually matter in a simple crossed-polarizer measurement of light-valve contrast, but can be important in analyzing the interaction with an optical system.

**Figure 5** shows schematically the  $n_e$  axis twisting from top to bottom of an LC layer, with  $\alpha$  the total twist angle. (In **Figure 5**  $\alpha$  is  $+45^\circ$ .) We use  $(E_x, E_z)$  as the Jones vector, and use the sign convention where waves oscillate as  $\exp[+iky - i\omega t]$ . Following Yariv and Yeh [19], we introduce a rotating coordinate system that tracks the twisting LC molecules; we then write the single-pass Jones matrix  $M_{LC}$  for the LC layer in dark state as the result of propagation through a large number  $N$  of birefringent slabs with progressively twisting orientation:



Figure 5

$$M_{LC} = \lim_{N \rightarrow \infty} R \begin{pmatrix} N-1 & \\ & 1 \end{pmatrix} \left[ \Delta M R \begin{pmatrix} \alpha & \\ & - \end{pmatrix} \right]_1^N \Delta M, \quad (1)$$

where  $\Delta M$  and  $R(\theta)$  are respectively defined as

$$\Delta M \equiv \begin{pmatrix} e^{i(\beta/N)} & 0 \\ 0 & e^{-i(\beta/N)} \end{pmatrix} \text{ and } R(\theta) \equiv \begin{pmatrix} \cos \theta & -\sin \theta \\ \sin \theta & \cos \theta \end{pmatrix}. \quad (2)$$

Here  $\beta$  is one half the integrated birefringence across the thickness  $D$  of the LC layer;  $\beta \equiv \pi (n_e - n_o)D/\lambda$  [ $n_e$  and  $n_o$  are the indices of refraction for the extraordinary and ordinary rays, respectively; they apply for the particular  $\gamma$ -tilt of the LC molecule (assumed not to vary with depth  $y$  when the light valve is in dark state)].

One way to evaluate the matrix exponential in Equation (1) is to use a generalized DeMoivre identity [20]:

$$(I \cos(\omega) + i\hat{n} \cdot \vec{\sigma} \sin(\omega))^m = (e^{i\omega\hat{n} \cdot \vec{\sigma}})^m = e^{im\omega\hat{n} \cdot \vec{\sigma}} = I \cos(m\omega) + i\hat{n} \cdot \vec{\sigma} \sin(m\omega), \quad (3)$$

where  $I$  is the identity matrix and  $\vec{\sigma}$  is a length-3 operator whose  $x$ ,  $y$ ,  $z$  components are the  $2 \times 2$  Pauli matrices  $\sigma_x$ ,  $\sigma_y$ , and  $\sigma_z$ :

$$\sigma_x \equiv \begin{pmatrix} 0 & 1 \\ 1 & 0 \end{pmatrix}, \quad \sigma_y \equiv \begin{pmatrix} 0 & -i \\ i & 0 \end{pmatrix}, \quad \sigma_z \equiv \begin{pmatrix} 1 & 0 \\ 0 & -1 \end{pmatrix}, \quad (4)$$

and where  $\hat{n}$  is an arbitrary unit vector.

Applying Equation (4) to Equation (1) and then applying Equation (3), we obtain almost by inspection the following very compact expression for the single-pass Jones matrix of a TNLC layer with zero applied voltage:

$$M_{LC} = e^{-i\alpha\sigma_y} e^{i(\alpha\sigma_y + \beta\sigma_z)}. \quad (5)$$

(Note that the exponents cannot simply be added because the matrices do not commute.) Using Equation (3) to cast Equation (5) into more familiar notation, we obtain the well-known result, appearing here with consistent signs:

$$M_{LC} = R(\alpha) \begin{pmatrix} \cos \gamma & \sin \gamma \\ \sin \gamma & \cos \gamma \end{pmatrix} e^{i\beta\sigma_z} \begin{pmatrix} \cos \gamma & \sin \gamma \\ \sin \gamma & \cos \gamma \end{pmatrix} e^{-i\alpha\sigma_y}, \quad (6)$$

$\gamma$  $\gamma$ 

where  $\gamma \equiv \sqrt{\alpha^2 + \beta^2}$ . We believe that Equation (6) shares its consistency in signs with results in, e.g., Reference [21], but not with, e.g., References [14, 19]. Note that a common phase factor is neglected in Equation (6).

To determine the double-pass matrix of the light valve, denoted  $M_{LV}$ , we must specify further details of our sign convention. In most of this paper we use the sign convention recently reviewed by Pistoni [22], in which, for Jones vector  $(E_x, E_z)$ , the  $x$ -axis unit vector is assumed to reverse direction in space after a normal-incidence reflection from a surface, while  $\hat{z}$  remains unchanged;  $\hat{y}$  is taken to point in the direction of travel of the ray, and so of course reverses direction also. In this convention,  $\hat{x}$ ,  $\hat{y}$ ,  $\hat{z}$  remains a right-handed triad after reflection. Unfortunately, this conflicts with the most common sign convention in thin-film coating design, where it is most often considered preferable that the  $S$  and  $P$  reflectivities converge to the same value at normal incidence.

In the right-hand-preserving convention, the matrix for the reversed path through a (lossless) element can be obtained very quickly from the matrix for the initial direction of propagation. Specifically, if  $M^{(rev)}$  denotes the reverse-path matrix, we have [22]

$$M_{(rev)} = \begin{pmatrix} m_{11} & -m_{21} \\ -m_{12} & m_{22} \end{pmatrix}, \quad (7a)$$

where the forward matrix is

$$M \equiv \begin{pmatrix} m_{11} & m_{12} \\ m_{21} & m_{22} \end{pmatrix}, \quad (7b)$$

Note that for our purposes only differential phases between  $S$ - and  $P$ -polarized components are important; absolute phase factors can be dropped. Similarly, Equation (7) will usually apply to a lossy element if the losses are equal in  $S$  and  $P$  polarizations. For such elements there are other symmetries we can exploit; for example, it is well known that their Jones matrices can always be expressed in such forms as

$$\begin{pmatrix} m_{11} & m_{12} \\ m_{21} & m_{22} \end{pmatrix} = \begin{pmatrix} \cos \mu e^{i\zeta} & \sin \mu e^{-i\zeta} \\ \sin \mu e^{i\zeta} & \cos \mu e^{-i\zeta} \end{pmatrix}$$

$$M = \begin{pmatrix} -m_{12}^* \\ m_{11}^* \end{pmatrix} \equiv M \begin{pmatrix} i\theta & \\ -\sin \mu e^{i\theta} & \cos \zeta \\ \mu e^{-i\zeta} & \end{pmatrix}, \quad (8a)$$

or

$$M \equiv \frac{1}{\sqrt{1 + |\mathbb{F}|^2}} \begin{pmatrix} e^{-i\theta} & \mathbb{F} e^{i\theta} \\ -\mathbb{F}^* e^{-i\theta} & e^{i\theta} \end{pmatrix}, \quad (8b)$$

where in the second expression  $\mu$ ,  $\zeta$ , and  $\theta$  are simply real parameters that enforce the required symmetries between the matrix elements. Complex parameter  $\mathbb{F}$ , in the last expression represents the output depolarization for a pure (0, 1) input; real  $\mathbb{F}$ , implies rotational depolarization and imaginary  $\mathbb{F}$ , elliptical depolarization. The depolarization is defined as  $(E_x/E_z)_{\text{output}}$  when  $\hat{E}_{\text{input}} = \hat{z}$ . [The phase factor  $\theta$  is canceled in calculating the depolarization.] Note that the polarization matrices of Equation (8) neglect common attenuation factors and common phase factors.

In our convention, the matrix for the light-valve bottom-surface mirror is  $-i\sigma_z$  [since we ignore common phase factors,  $-i$  is introduced to preserve the symmetry of Equation (8)], and, neglecting common phase factors, we can use Equations (6) and (7) to obtain the matrix for the dark-state TNLC light valve in reflection:

$$M_{LV} \equiv -i M_{LC}^{(\text{rev})} \sigma_z M_{LC}$$

$$= \begin{pmatrix} \frac{2\beta^2 \sin^2 \gamma}{\gamma^2} & \frac{2\alpha\beta \sin^2 \gamma}{\gamma^2} \\ \frac{2\alpha\beta \sin^2 \gamma}{\gamma^2} & \frac{2\beta^2 \sin^2 \gamma}{\gamma^2} \end{pmatrix} + \beta \left( \frac{\sin 2\gamma}{\gamma} \right) \begin{pmatrix} 1 & \\ - & \end{pmatrix} i \begin{pmatrix} 1 & \\ - & \end{pmatrix} + \beta \left( \frac{\sin 2\gamma}{\gamma} \right) \begin{pmatrix} 1 & \\ - & \end{pmatrix} i \begin{pmatrix} 1 & \\ - & \end{pmatrix} \quad (9)$$

$\gamma$ )

which is equivalent to the result of Lu and Saleh [14], except for sign corrections and conventions.

Projection optics that are designed to avoid deliberate depolarization of the beam will tilt surfaces only about rotation axes that are aligned either with, or perpendicular to, the illumination polarization of the central ray. Otherwise, any surface that is tilted by more than  $\sim 20^\circ$  (depending on the coating) is likely to produce a strong "zero-order" depolarization even in the central (i.e., principal) ray of the beam, because of differences in the phase or amplitude of  $S$  and  $P$  reflectance or transmittance. Even when surface tilts are restricted to the  $S$  or  $P$  axes of the central ray, compound-angle effects can cause first-order depolarization in off-center rays; this depolarization scales linearly with the difference in skew propagation angle between the off-center ray and the principal ray (linear in amplitude, quadratic in intensity).

For the central ray, however, the curves of Figures 1 and 2 suggest that the PBS-based optical system (with supplemental sheet polarizer) is almost equivalent to ideal crossed polarizers. The light valve then contributes a residual dark-state intensity equal to the square of the off-diagonal elements in Equation (9). In practice, the TN light valve should have non-negligible LC birefringence, so parameter  $\beta$  is unlikely to be small. The off-diagonal elements are zero at  $\gamma = \pi$ , i.e., at  $\beta = \sqrt{\pi^2 - \alpha^2}$ . (For simplicity, the case in which  $\gamma$  equals a larger multiple of  $\pi$  is not considered here.) One consideration in choosing the twist angle  $\alpha$  is that a high polarization conversion efficiency be obtained when the light valve is driven to maximum brightness;  $\alpha = 45^\circ$  is a possible choice [23]. Usually  $\beta \equiv \pi (n_e - n_o)D/\lambda$  will only reduce to  $\sqrt{m^2\pi^2 - \alpha^2}$  at a single wavelength within the spectral band illuminating the light valve (i.e., where  $m = 1$ ). The light valve background scales with approximately the fourth power of small wavelength shifts away from the center wavelength, as illustrated in Figure 6. It should be noted that liquid crystal materials are often highly dispersive in birefringence;  $\Delta n \equiv n_e - n_o$  might change by -0.5% for every 1% increase in  $\lambda$ . A more detailed treatment of TNLC reflective light valves is given by Yang and Lu [24].



Figure 6

### Optical system

The compound-angle properties of a PBS are generic in the sense that the desired  $S$ ,  $P$  performance of such a coating is in itself sufficient to approximately determine the depolarization the coating imposes on skew rays; to wit, the PBS rotates skew-ray polarization by an angle equal to

the rotation between the incident and return planes of incidence (as shown in [Figure 3](#)). Color-separating coatings like that in [Figure 4](#) also have a simple performance target, namely that within a particular color band either their reflectance or their transmittance should approach unity. This efficiency goal is usually satisfied fairly well by practical coatings, meaning that at most wavelengths within the color band the coatings will not be amplitude polarizers. Tilted dichroic coatings will be strong amplitude polarizers at the edges of the band, which means that they will tend to be strong phase polarizers throughout the band. (Compactness considerations generally require that the beam be folded at fairly steep angles of incidence.) From an efficiency point of view one would require that the *S* and *P* reflectance (or transmittance) be close to unity over most of the band, and that the split between the *S* and *P* band edges be as narrow as possible. This represents a qualitative description of the coating's intensity response, and in principle coating phase shifts can be significantly determined by a complete description of the intensity response at all wavelengths [25]. However, in practice the knowledge that available coatings are likely to show high efficiency over most of the band is not sufficient to draw conclusions about phase properties of the coatings. For one thing, designs for tilted color splitters that show low intensity polarization generally achieve this at only one edge of the band [26], whereas the dispersion integrals that link coating intensity and coating phase shift extend over the full spectrum, with a kernel that changes fairly slowly. Second, these dispersion integrals involve the logarithm of the intensity response; a tilted coating would usually be regarded as adequately nonpolarizing in intensity if, for example, the theoretical *S* transmittance were  $10^{-4}$  and the theoretical *P* transmittance  $10^{-2}$ , but in such cases the log transmittances still differ appreciably, giving rise to significant *S*-*P* relative phase shifts. (The usual "nonpolarizing" edge filter is in fact still polarizing at the band edge when evaluated on a dB scale.) The *S*-*P* phase shifts cause depolarization through the optical system, but, in contrast to the case with the PBS, their effect cannot be calculated or even well estimated without detailed coating prescriptions. The phase shift from dichroic coatings is often appreciable, however. In the center of the reflection band, the first few layers of the coating are sufficient to almost extinguish the transmitted beam, while wavelengths near the band edge penetrate almost to the exit medium. Color-splitting coatings tend to be fairly thick, and for angles of incidence  $\gtrsim 20^\circ$  there is generally some difference in effective penetration depth between the *S* and *P* components, making the coating a phase polarizer.

Specific coating calculations are outside the scope of the present paper. However, we show in this paper that in a first-order calculation we can define a specific depolarization contribution that is introduced by an individual coated surface; we can then propagate the depolarization as a single quantity from surface to surface. This formulation proves convenient for analyzing the interaction of the optics with the light valve. In the present section of this paper we apply the most common sign

convention in thin-film design (see for example Figures 2.1 and 2.2 of Thelen [26]), in which amplitude-reflection coefficients are positive when the projections onto the reflecting interface of  $\vec{E}_{\text{Incident}}$  and  $\vec{E}_{\text{reflected}}$  are parallel and negative when antiparallel. (The same convention is used for the transmission coefficients.) We use (0) as a superscript to denote quantities referring to the principal ray (i.e., the central ray of the beam). If  $\hat{w}_i^{(0)}$  represents the direction of the central ray incident on the  $i$ th surface, and  $\hat{s}^{(0)}$  is a unit vector that defines the direction of S polarization, it is customary in thin-film calculations to choose the sign of  $\hat{s}^{(0)}$  according to  $\hat{s}_{i+1}^{(0)} \equiv \hat{s}_i^{(0)} \equiv (\hat{w}_i^{(0)} \times \hat{w}_{i+1}^{(0)})/|\hat{w}_i^{(0)} \times \hat{w}_{i+1}^{(0)}|$ , where  $\hat{w}_{i+1}^{(0)}$  is the reflected ray; thus, the same  $\hat{s}^{(0)}$  is used for the incident, reflected, and transmitted rays. The  $E$ -field direction in  $P$  polarization is then most commonly set to  $\hat{p}_i^{(0)} \equiv \hat{s}_i^{(0)} \times \hat{w}_i^{(0)}$  for the incident ray, for the reflected ray to  $\hat{p}_{i+1}^{(0)} \equiv -\hat{s}_{i+1}^{(0)} \times \hat{w}_{i+1}^{(0)}$ , and for the transmitted ray to  $\hat{p}_{i+1}^{(0)} \equiv \hat{s}_{i+1}^{(0)} \times \hat{w}_{i+1}^{(0)}$ . In this convention  $\hat{s}$ ,  $\hat{w}$ , and  $\hat{p}$  are not preserved as a right-hand triad, but the  $S$  and  $P$  reflectances converge to the same value at normal incidence.

We have found proper interpretation of signs to be one of the most time-consuming aspects of correctly calculating depolarization through an optical system. Standard thin-film formalisms serve as a convenient standard for defining the change in electric field at a coated surface. Given the amplitude reflectance  $\rho$  and transmittance  $\tau$  of a coated surface, it is straightforward to propagate the  $E$ -field from one surface to the next. Applying the Fresnel equation for reflection,

$$\vec{E}_{i+1} = \rho_S(\vec{E}_i \cdot \hat{s}_i)\hat{s}_i + \rho_P(\vec{E}_i \cdot \hat{s}_i \times \hat{w}_i)(\hat{w}_{i+1} \times \hat{s}_i),$$

$$= \frac{\hat{w}_i \times \hat{g}_i}{|\hat{w}_i \times \hat{g}_i|} \cdot \hat{s}_i,$$

$$\hat{w}_{i+1} = \hat{w}_i - 2(\hat{w}_i \cdot \hat{g}_i)\hat{g}_i, \quad (10)$$

where  $\hat{g}_i$  is the surface normal; and for transmission,

$$\begin{aligned} \vec{E}_{i+1} = & \tau_p (\vec{E}_i \cdot \hat{s}_i) \hat{s}_i - \frac{\hat{w}_i \cdot \hat{q}_i}{|\hat{w}_{i+1} \cdot \hat{q}_i|} (\vec{E}_i \cdot \hat{s}_i \times \hat{w}_i) (\hat{w}_{i+1} \times \hat{s}_i), \\ \hat{s}_i = & \frac{\hat{w}_i \times \hat{q}_i}{|\hat{w}_i \times \hat{q}_i|}, \\ \hat{w}_{i+1} = & (\hat{w}_i \cdot \hat{q}_i) \hat{q}_i \sqrt{\frac{(1 - (n_i^2/n_{i+1}^2))}{(\hat{w}_i \cdot \hat{q}_i)^2} + \frac{n_i^2}{n_{i+1}^2}} - \frac{n_i}{n_{i+1}} (\hat{w}_i \times \hat{q}_i) \times \hat{q}_i, \end{aligned} \quad (11)$$

where  $n_i$  and  $n_{i+1}$  are the refractive indices. As is usual in thin-film calculations,  $\tau$  in Equation (11) refers to the tangential components of the  $E$ -field. The square root in Equation (11) is always taken to be positive. Equations (10) and (11) are expressed in a form that is independent of whether  $\hat{q}_i$  is chosen to point "in" to or "out" from the surface (making numerical ray-trace calculations more straightforward), hence the somewhat complicated form chosen for Snell's law in the third line of Equation (11).

Equations (10) and (11) define the electric field throughout the optical system when standard thin-film algorithms are used to calculate the transfer coefficients  $\rho$ ,  $\tau$  at the surfaces. The  $x$ ,  $y$ ,  $z$  components of the  $E$ -field are defined in the same global coordinate system as the ray vectors  $\hat{w}_i$  and surface normals  $\hat{q}_i$ . The equations thus serve as a convenient basis for developing simpler, closed-form solutions [e.g., Equations (19) and (22) below] that maintain a consistent and easily visualized sign convention throughout the system. These first-order solutions can also be derived in a heuristic way, as outlined in the caption of **Figure 7**.

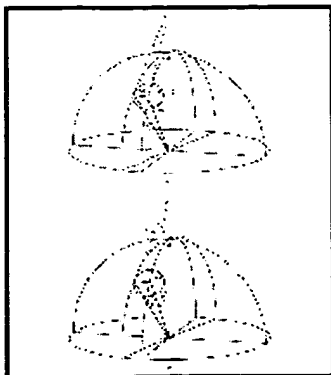


Figure 7



Equations (10) and (11) can also be used in numerical calculations as an alternative to the matrix-based approaches described in the literature (e.g., Waluschka [11]). We pursue them here in order to derive a closed-form first-order equation that propagates the beam depolarization from surface to surface. We have found this first-order analysis to be quite accurate for NAs of interest ( $NA \approx 0.14$ ); in addition, examination of the depolarization contributed by a surface provides useful insight into the nature of the compound-angle contrast loss. The depolarization contributed by a surface to a ray is for our purposes the quantity of direct interest.

A surface-specific beam depolarization should probably only be considered a well-defined quantity in a first-order analysis, because it is only to first order that one can speak of a generic linear polarized beam of finite NA that can serve as a reference. One might arbitrarily choose, for example, a linear dipole pattern as a reference for the general case, but this is a somewhat arbitrary choice, and it would give rise to higher-order terms in the calculated depolarization that would be specific to that choice. However, when the surface is tilted, a unique first-order contribution can be identified.

Consider, for example, reflection of a nominally S-polarized beam whose central ray is pure S-polarized. Figures 7(a) and 7(b) show the reflecting surface as horizontal, with surface normal  $\hat{q}$  pointing upward. We can always find quantities  $E_0$ ,  $\delta E_{i,L}$ , and  $\delta E_{i,P}$  ( $\delta E_{i,L}$  and  $\delta E_{i,P}$  are small) that will express the  $E$ -field of a particular ray in the beam according to

$$\vec{E}_i = E_0 \hat{s}_i + \delta E_{i,L} \hat{w}_i + \delta E_{i,P} (\hat{w}_i \times \hat{s}_i), \quad (12)$$

because  $\hat{s}_i$ ,  $\hat{w}_i$ , and  $(\hat{w}_i \times \hat{s}_i)$  form an orthonormal set. Of course  $\delta E_{i,L}$  must equal zero in order that Equation (12) preserve the transversality of the  $E$ -field (so that  $\vec{E}_i \cdot \hat{w}_i = 0$ ); however,  $\delta E_{i,L}$  becomes nonzero in a first-order expansion (see below). Also, to first order the magnitude squared of Equation (12) is  $E_0^2$ , so that  $E_0 \cong E_i$ . (In assuming that the depolarization is small compared to that of the overall  $E$ -field, we are assuming for the time being that  $\rho_S$  is large enough that the beam remains predominantly S-polarized after reflection from the surface.) When the skew angle is small, we then have

$$\vec{E}_i \cong E_i [\hat{s}_i^{(0)} - (\delta \vec{w}_i \cdot \hat{s}_i^{(0)}) \hat{w}_i^{(0)}] + \delta \vec{E}_{i,P} (\hat{w}_i^{(0)} \times \hat{s}_i^{(0)}), \quad (13)$$

$$\frac{\delta \vec{w}_i}{\hat{w}_i^{(0)}} \approx \hat{w}_i \quad (14)$$

represents the propagation angle of the ray within the NA [see Figure 7 (a)]. In deriving Equation (13) from Equation (12) we have set  $\delta E_{i,L}$  equal to  $E_0(\delta \vec{w}_i \cdot \hat{s}_i^{(0)})$ , in order that  $\vec{E}_i \cdot \hat{w}_i \equiv \vec{E}_i \cdot (\hat{w}_i^{(0)} + \delta \vec{w}_i) = 0$  to first order.

Expanding the second equation in Equation (10), we find, after some algebra,

$$\hat{s}_i \cong \hat{s}_i^{(0)} - (\hat{s}_i \cdot \hat{w}_i^{(0)}) \frac{(\hat{w}_i^{(0)} \cdot \hat{s}_{i+1}^{(0)})}{|\hat{q}_i \times \hat{w}_i^{(0)}|} \quad (15)$$

where we have deliberately mixed quantities involving  $\hat{w}_i$  and  $\hat{w}_{i+1}$ . Similarly,

$$\hat{s}_{i+1}^{(0)} \cdot \delta \vec{w}_{i+1} \cong \hat{s}_i^{(0)} \cdot \delta \vec{w}_i, \quad \vec{E}_i \cdot \hat{s}_i \cong E_i, \quad \hat{w}_i \cong - \frac{(\hat{s}_i^{(0)} \cdot \hat{s}_{i+1}^{(0)})}{|\hat{q}_i \times \hat{w}_i^{(0)}|} \quad (16)$$

If  $\vec{E}_{i+1}$  is expressed in the form taken by  $\vec{E}_i$  in Equation (13), and then substituted with Equations (13), (15), and (16) into the first line of Equation (10), we obtain in first order

$$\hat{q}_i \cdot \hat{w}_i$$

$$\frac{\delta E_{i+1,P}}{E_{i+1}} = \frac{\rho_P}{\rho_S} \frac{\delta E_{i,P}}{E_i} + \left( -\frac{1}{1} \right) \frac{(\hat{s}_i^{(0)} \cdot \delta \vec{w}_i)}{|\hat{q}_i \times \hat{w}_i^{(0)}|} \quad (17)$$

The left side of Equation (17) is the cumulative depolarization introduced in the nominally S-polarized beam by the  $i$ th reflection (and by previous tilted coatings). The factor  $\rho_P/\rho_S$  will be a phase factor if the  $i$ th surface is lossless (or has equal intensity loss in the two polarizations); this would be the case for a dichroic coating away from the band edge. The  $\rho_P/\rho_S$  factor multiplies any depolarization that may be present in the ray from previous surfaces. The last term on the right can be thought of as the incremental depolarization contributed by skew angle incidence at the  $i$ th surface. If the angle of incidence of the central ray is  $\varphi_0$ , then the skew angle  $\theta_i \equiv \hat{s}_i^{(0)} \cdot \delta \vec{w}_i$  of the ray is the component of the ray tilt that lies in the direction perpendicular to  $\varphi_0$  [see Figure 7(b)]. Within the skew meridian, the angle of incidence remains unchanged to first order. Note that while Figure 7 shows  $\delta \vec{w}_i$  for the case of a pure skew ray,  $\hat{s}_i^{(0)} \cdot \delta \vec{w}_i = \theta_i$  in Equation (17) can represent the skew component of any ray; also, a purely meridional ray at one tilted surface may be a pure skew ray at another surface.

The last term in Equation (17) shows that a tilted surface introduces a depolarization that is linear (in amplitude) with skew angle  $\theta_i$ . This term contains a factor

$$\chi \equiv \frac{(\hat{s}_i^{(0)} \cdot \delta \vec{w}_i)}{|\hat{q}_i \times \hat{w}_i^{(0)}|} = \frac{\theta_i}{\tan \varphi_0}, \quad (18)$$

which is the angle of rotation between the directions of pure  $P$  polarization for the ray and for the central ray [see Figure 7(b)]. The remaining factor

in the depolarization term,  $(\rho_p/\rho_s) - 1$ , implies that even when the  $E$ -field has projections in both the  $S$  and  $P$  planes, first-order compound-angle depolarization will not take place unless the coating is actually polarizing. This coating factor has a maximum magnitude of 2 (for a coating with  $180^\circ$  S/P phase shift); this is twice as large in amplitude (four times larger in intensity) as the value from a PBS intensity polarizer.

The  $(\tan \varphi_0)^{-1}$  dependence of  $\mathcal{X}$  in Equation (18) leads to the surprising result that shallow angles of incidence can produce more severe depolarization than steep incidence. Of course, as  $\varphi_0 \rightarrow 0$  (where our expansion breaks down), a surface becomes nonpolarizing, but for angles of incidence as small as, e.g.,  $30^\circ$  (depending on  $n_i$ ), the S-P phase shift from a dichroic coating can take on essentially any value between 0 and  $2\pi$ . Since intensity depolarization scales as amplitude squared, a  $30^\circ$  tilted surface can introduce appreciably more depolarization than, say, a  $45^\circ$  surface.

Equation (17) is readily generalized. For example, if many tilted surfaces are traversed, all in a two-dimensional layout, and we consider the tilt of the  $i$ th surface to arise from rotation of the surface about an axis parallel to  $\hat{s}_i^{(0)}$ , then because the layout is two-dimensional, these tilt axes will all be parallel to the tilt axis  $\hat{s}_{\text{PBS}}^{(0)}$  of the PBS. In this case we find that for each surface,

$$\frac{\delta E_{i+1}}{E_{i+1}} = \xi_i \left[ \frac{\delta E_i}{E_i} - \frac{\kappa_i (\eta_i - \eta_i^{-1})}{n_i \tan \varphi_{0,i}} \frac{\theta_0}{n_i \tan \varphi_{0,i}} \right], \quad (19)$$

where  $\xi_i = +1$  if the ray follows the transmitted path through the surface, and  $-1$  if it follows the reflected path.  $\eta_i$  is defined as  $(\rho_p/\rho_s)$  for a reflected ray and as  $(\tau_p/\tau_s)$  for a transmitted ray.  $n_i$  is the refractive index in the incident space at the  $i$ th surface, and  $\theta_0$  is the skew angle of the ray as measured in air.  $\theta_0$  is invariant through the system. The beam angle of incidence  $\varphi_{0,i}$  is always taken as positive. The sign of the surface depolarization is governed by parameter  $\kappa$ , which essentially specifies whether the surface tilt is oriented so as to deviate the reflected ray clockwise or counterclockwise;  $\kappa$  is defined as

$$+1 \text{ if } \hat{w}_i^{(0)} \times \hat{w}_{i+1}$$

$$\kappa_i \equiv \begin{cases} {}^{(0)} \cdot \hat{s}_{\text{PBS}}^{(0)} > 0, \\ -1 \text{ if } \hat{w}_i^{(0)} \times \hat{w}^{(0)} \\ {}_{i+1} \cdot \hat{s}_{\text{PBS}}^{(0)} < 0. \end{cases} \quad (20)$$

[Note that the  $\hat{w}_{i+1}^{(0)}$  appearing in Equation (20) always refers to the reflected ray, even when the depolarization is being calculated for the transmitted beam.]

In the general case where the layout is not two-dimensional, i.e., at least one surface  $i$  is tilted about the axis perpendicular to the tilt axis of the PBS hypotenuse, Equation (19) still applies if 1) the angle  $\theta_0$  is replaced by  $\psi_0$ , again defined as  $\hat{s}_i^{(0)} \cdot \hat{s}\vec{w}_i$  (which for an orthogonally tilted surface will be in the meridian perpendicular to  $\theta_0$ ), 2) parameter  $\eta_i$  is defined as  $\rho_S/\rho_P$  or  $\tau_S/\tau_P$ , and 3) the definition of  $\kappa_i$  in Equation (20) is multiplied by -1.

Equation (19) can be rewritten in a number of ways; for example, we can propagate the depolarization in the ray relative to the tilted ray-specific  $P$  direction according to

$$\left( \frac{\delta E}{E} - \frac{\theta_0 \kappa}{n \tan \varphi_0} \right)_{i+1} = \xi_i \eta_i \left( \frac{\delta E}{E} - \frac{\theta_0 \kappa}{n \tan \varphi_0} \right)_i - \theta_0 \left[ \frac{\kappa_{i+1}}{n_{i+1} \tan \varphi_{0,i+1} - \kappa} - \frac{\kappa_i \xi_i}{n_i \tan \varphi_{0,i}} \right]. \quad (21)$$

If the  $i$ th and  $i+1$ th surfaces are parallel and in the same medium, the term in square brackets is zero (because  $\kappa_{i+1} = \kappa_i \xi_i$  when the surfaces are parallel); in such a case Equation (21) shows that the surface contributes no relative depolarization.

As a linear difference equation, Equation (19) is easy to solve for an arbitrary succession of  $j = 0, \dots, J$  tilted interfaces (starting from  $j = 0$  at the PBS). The closed-form solution is

$$\frac{\delta E_{J+1}}{E_{J+1}} = - \left( \prod_{j=1}^J \xi_j \eta_j \right) \kappa_0 \frac{\theta_0}{n_{\text{PBS}}} - \sum_{j=1}^J \left[ \xi_j \kappa_j (\eta_j - 1) \left( \prod_{k=j+1}^J \xi_k \eta_k \frac{\theta_0}{n_k \tan \varphi_{0,k}} \right) \right] \quad (22)$$

We should note that Equations (19) and (22) have one limitation that is not easily generalized out. If the beam path includes tilted interfaces at

which the rays are transmitted, these interfaces must arise in pairs analogous to the front and back surface of a tilted parallel plate; i.e., a tilted transmission interface must be followed by a parallel transmission interface, and the exit refractive index must equal the incident index at the first interface. The intervening space can then be treated as a thick incoherent layer. Thus, the first-order formalism applies to a tilted air space, or to front-side and back-side coatings on a tilted dichroic mirror, but not to a refractive prism. Elements with wedge give rise to strong aberrations and so would not ordinarily be used in a projection display; Equations (10) and (11) are available for numerical solution in such a case. [Equations (19) and (22) have no restriction on traversal of interfaces at angles near normal incidence, i.e., interfaces that are only slightly tilted.]

#### *Contrast loss from interaction between light valve and optical system*

The methods of the previous section can be used to propagate the  $E$ -field to and from the light valve. An earlier section presented analysis to account for the polarization properties of the light valve itself. Together these constitute a solution for the contrast loss through the optical system. However, with one further restriction we can establish solutions that are easily written in a simpler and more compact form, but which still represent fairly general descriptions of the interaction. So long as the only lossy element in the path is the PBS (the PBS is lossy in the sense that it directs some light into a different path), we show that we can describe the interaction with the light valve purely in terms of the rotation and ellipticity that the optics induce on the illumination. Under this restriction we treat coatings in the system other than the PBS as phase polarizers;  $\rho_P = e^{i\Delta_P}$  and  $\rho_S = e^{i\Delta_S}$ . As noted above, the optical coatings in a given color channel are designed to be as efficient as possible, and losses are usually small except at the edges of the band. We have found in numerical calculations that phase effects often dominate over amplitude effects even near the band edges, and the accuracy of the phase-only approximation becomes quite good when dark-state intensity contributions are integrated over the entire color band.

The assumption of lossless elements (or, more precisely, the assumption that elements have equal loss in  $S$  and  $P$  polarization) is not necessary in using the equations of the previous sections. The advantage of such an assumption is that it allows us to employ the symmetries in Equations (7) and (8). Unfortunately, while Equation (19) is based on the most common sign convention in thin-film design (see, for example, Thelen [26]), the most common Jones-matrix sign convention [22] is incompatible because it preserves as a right-handed triad the two polarization basis directions and the ray direction. To express Equation (19) in the matrix sign convention, we briefly adopt a somewhat awkward notation in order to introduce absolute phase factors that maintain the symmetry of Equation (8) independent of whether  $\xi$  equals +1 or -1. Specifically, we write  $i$  in

the form  $i = \sqrt{\xi}$  for the case  $\xi = -1$ ; when  $\xi = +1$ , this  $\sqrt{\xi}$  factor is unity. The Jones-matrix form of Equation (19) can then be written:

$$\begin{pmatrix} \delta E_{i+1} \\ E_{i+1} \end{pmatrix} = \sqrt{\xi_i} e^{i(\Delta_P + \Delta_S)/2} \begin{pmatrix} \sqrt{\xi_i} e^{i(\Delta_P - \Delta_S)/2} & 2 \frac{\kappa_i}{\sqrt{-\xi_i}} \sin\left(\frac{\Delta_P - \Delta_S}{2}\right) \frac{\theta_0}{n_i \tan \varphi_{0,i}} \\ -2 \sqrt{-\xi_i} \kappa_i \sin\left(\frac{\Delta_P - \Delta_S}{2}\right) \frac{\theta_0}{n_i \tan \varphi_{0,i}} & \frac{e^{-i(\Delta_P - \Delta_S)/2}}{\sqrt{\xi_i}} \end{pmatrix} \begin{pmatrix} \delta E_i \\ E_i \end{pmatrix}. \quad (23)$$

Note that Equation (23) is in a form in which an additional matrix for rotation of the  $S$ ,  $P$  axes to propagate to the next surface is unnecessary. Equation (23) is most naturally associated with a different sign convention from that of Equation (19); the difference is essentially that in Equation (23) the projections onto the surface of the reflected and incident unit vectors  $\text{prefl}$ ,  $\text{pinc}$  for  $P$  polarization are antiparallel. The  $\sqrt{\xi}$  factor outside the matrix is included in Equation (23) for consistency with Equation (19); however, since its value is either  $i$  or  $1$ , it represents a common phase factor and can be dropped;  $e^{i(\Delta_P + \Delta_S)/2}$  is likewise a common phase factor. In this part of the paper we assume equal efficiency in  $S$  and  $P$  polarizations; any common attenuation factor is also dropped if system contrast is the quantity of interest.

The diagonal elements of the matrix of Equation (23) have magnitude unity; the off-diagonal elements are first-order quantities proportional to the skew angle  $\theta_0$ . When two such matrices are multiplied together, the product matrix preserves this structure to first order. An equivalent statement is that the multisurface solution in Equation (22) exhibits this form when written as a matrix.

Since the optical system should not depolarize the central ray, we can assume that all surfaces are tilted about axes that are either parallel to the  $\hat{s}^{(0)}_{\text{PBS}}$  tilt axis of the PBS hypotenuse, or are perpendicular to it. A ray can be parametrized by the skew angle  $\theta_0$  it makes to the PBS hypotenuse (scaled for air,  $n = 1$ ), and by an orthogonal angle  $\psi_0$ .  $\theta_0$  and  $\psi_0$  thus represent an orthogonal pair of pupil coordinates which range between  $-NA$  and  $+NA$  (with  $\sqrt{\theta_0^2 + \psi_0^2} \leq NA$ ). Excluding the PBS, the Jones matrix for the optical system then takes the form

$$M_{\text{Non-PBS optics}} = \begin{pmatrix} e^{i\pi/2} & v_{\theta\theta} \theta_0 + v_{\psi\psi} \psi_0 \\ -v_{\theta\theta}^* \theta_0 - v_{\psi\psi}^* \psi_0 & e^{-i\pi/2} \end{pmatrix}, \quad (24)$$

where  $v_\theta$ ,  $v_\psi$ , and  $\Sigma$  are determined by the methods of the previous section. In first order the illumination matrix for the PBS is

$$M_{\text{PBS}} = \begin{pmatrix} 0 & -\theta'_0 \\ \theta_0 & 1 \end{pmatrix}, \quad (25)$$

where  $\theta'_0 \equiv \theta_0/n_{\text{PBS}}$  is the skew angle of incidence inside the PBS. (For the time being we assume a 45° cube PBS.) Assuming as an input, for example, unpolarized light, the Jones vector for the  $E$ -field illuminating the light valve

will then take the form

$$\begin{pmatrix} \delta E \\ E \end{pmatrix} \cong \begin{pmatrix} -\theta_0 e^{i\Sigma/2}/n_{\text{PBS}} + v \\ \theta_0 \theta_0 + v_\psi \psi_0 \\ e^{-i\Sigma/2} \end{pmatrix}, \quad (26)$$

where second-order terms are dropped. The depolarization of the illumination then takes the form

$$\frac{\delta E}{E} = -\theta_0 [e^{i\Sigma}/n_{\text{PBS}} - v_\theta e^{i\Sigma}/2] + \psi_0 [v_\psi e^{i\Sigma/2}]. \quad (27)$$

For small depolarization, the real part of  $\delta E/E$  represents a rotation in the illuminating polarization and the imaginary part an ellipticity. According to Equation (27), a ray in the skew meridian to the PBS ( $\psi_0 = 0$ ) will have rotation and ellipticity that are proportional to  $\theta_0$ , while for a ray in the orthogonal meridian, rotation and ellipticity will be proportional (with different constants of proportionality) to  $\psi_0$ . Let us denote these constants of proportionality as  $\Re_\theta$ ,  $\Im_\theta$ ,  $\Re_\psi$ ,  $\Im_\psi$ .  $\Re$  represents rotation in the sense that the optical coatings introduce  $\Re$  radians of polarization rotation per radian of skew angle in a ray illuminating the light valve; similarly, the induced ellipticity is  $\Im$  in the sense that the aspect ratio of a rectangle which circumscribes the polarization ellipse will be  $\Im_\theta$  when the ray skew angle is  $\theta$  ( $\theta$  assumed small). Note that while rotation and ellipticity are considered small (proportional to  $\theta$ ,  $\psi$ ), the constants of proportionality  $\Re$ ,  $\Im$  may have appreciable magnitude.



We now can write Equation (24) as

$$\begin{aligned} M_{\text{Non-PBS optics}} &= \begin{pmatrix} 1 & \mathcal{P}_\theta \theta_0 + \mathcal{P}_\psi \psi_0 \\ -\mathcal{P}_\theta & \\ \theta_0 - \mathcal{P}_\theta & 1 \\ \psi \psi_0 & \end{pmatrix} M_{\text{OptPhase}}, \end{aligned} \quad (28)$$

where

$$\begin{aligned} \mathcal{P}_\theta &\equiv (\Re_\theta + i\Im_\theta) e^{i\Sigma} \\ /n_{\text{PBS}} &= v_\theta e^{-i\Sigma/2}, \\ \mathcal{P}_\psi &\equiv (\Re_\psi + i\Im_\psi) = v_\psi e^{-i\Sigma} \\ /2, \end{aligned} \quad (29)$$

and

$$M_{\text{OptPhase}} \equiv \begin{pmatrix} e^{i\Sigma/2} & 0 \\ 0 & e^{-i\Sigma/2} \end{pmatrix}. \quad (30)$$

Equation (29) obtains because, when substituted [together with Equation (30)] into Equation (28) and compared with Equation (24), the expressions obtained for  $v_\theta$ ,  $v_\psi$  give the correct result when substituted into Equation (27), namely  $\delta E/E = (\Re_\theta + i\Im_\theta)\theta_0 + (\Re_\psi + i\Im_\psi)\psi_0$ ; we have defined the parameters  $\Re_\theta$ ,  $\Im_\theta$ ,  $\Re_\psi$ ,  $\Im_\psi$  by the requirement that the depolarization  $\delta E/E$  take this form. In other words, Equations (28)-(30) represent the optical system in terms of the rotation  $\Re$  and ellipticity  $\Im$  it imposes on skew rays incident at the light valve.

We now represent  $M_{\text{PBS}}$  [Equation (25)] as

$$\begin{aligned} M_{\text{PBS}} &= \begin{pmatrix} 0 & -\theta_0/n_{\text{PBS}} \\ \theta_0/n_{\text{PBS}} & 1 \end{pmatrix} \Rightarrow M_{\text{Rot}} M_{\text{PrePol}}, \end{aligned} \quad (31)$$

where

$$M_{\text{Rot}} \equiv \begin{pmatrix} 1 & -\theta_0/n_{\text{PBS}} \\ \theta_0/n_{\text{PBS}} & 1 \end{pmatrix}$$

$$M_{\text{PrePol}} \equiv \begin{pmatrix} 0 & 0 \\ 0 & 1 \end{pmatrix}. \quad (32)$$

Note that  $M_{\text{PrePol}}$  is taken to represent part of the PBS operation. The projector might also include a sheet polarizer (at least in the reflection pass) to ensure adequate rejection, but with or without such a supplementary polarizer the system must perform an operation equivalent to  $M_{\text{PrePol}}$ .

Using Equation (31), we can now write the first-order matrix for the optics (illuminating in single pass) as

$$\begin{aligned} M_{\text{Optics}} &= M_{\text{Non-PBSoptics}} M_{\text{PBS}} \\ &\equiv M_{\text{OpticsAll}} M_{\text{PrePol}}, \end{aligned} \quad (33)$$

where  $M_{\text{OpticsAll}}$  combines the  $M_{\text{Rot}}$  rotation from the PBS [Equation (32)] with the non-PBS optical elements [ $M_{\text{Non-PBSoptics}}$  given in Equations (24) and (28)], and can be written as

$$M_{\text{OpticsAll}} \equiv M_{\text{Perturb}} M_{\text{OptPhase}}, \quad (34)$$

where

$$M_{\text{Perturb}} \equiv \begin{pmatrix} 1 & [\Re_{\theta} + i\Im_{\theta}]\theta_0 + [\Re_{\psi} + i\Im_{\psi}]\psi_0 \\ -[\Re_{\theta} - i\Im_{\theta}]\theta_0 - [\Re_{\psi} - i\Im_{\psi}]\psi_0 & 1 \end{pmatrix}, \quad (35)$$

and where  $M_{\text{OptPhase}}$  is defined in Equation (30). For compactness we now introduce a vector notation for the pupil coordinates in which we denote the ray-propagation angle as  $\hat{\theta} \equiv (\theta_0, \psi_0)$ . Defining

$$\hat{P} \equiv \hat{R} + i\hat{I} \equiv ([\Re_{\theta} + i\Im_{\theta}], [\Re_{\psi} + i\Im_{\psi}]), \quad (36)$$

we have

$$M_{\text{Perturb}} = \begin{pmatrix} 1 & \hat{P} \cdot \hat{\theta} \\ 0 & 1 \end{pmatrix}. \quad (37)$$

$$= \begin{pmatrix} -\hat{P}^* \cdot \hat{\theta} & 1 \\ \hat{\theta} & \end{pmatrix}$$

$\hat{P} \cdot \hat{\theta}$  is the depolarization  $\delta E/E$  in the light incident on the light valve. The single (illumination)-pass matrix for the optical system is now

$$M_{\text{Optics}} = M_{\text{Perturb}} M_{\text{OptPhase}} M_{\text{PrePol}} \quad (38)$$

To propagate through the system in double pass (illumination and collection), we must determine the matrix for reverse propagation along the sequence of Equation (38). All component matrices in Equation (38) except for  $M_{\text{PrePol}}$  are assumed to exhibit equi-S-P efficiency. We first note, therefore, that given our sign convention the matrices other than  $M_{\text{PrePol}}$  are reversible in a strict sense according to the rule of Equation (7) above. For example, if we were to apply Equation (7) directly to Equation (37) we would obtain

$$M_{\text{Perturb}}^{(\text{rev})} = \begin{pmatrix} 1 & \hat{P}^* \cdot \hat{\theta} \\ -\hat{P} & 1 \\ \hat{\theta} & \end{pmatrix}. \quad (39)$$

However, Equation (7) applies to a true "time reversal," in which the rays are made to exactly retrace their incoming paths. In a projector, the rays that reflect from the light valve return to the optical system through the opposite side of the lens pupil. As noted in the introduction, this means that the optics obey a reversal symmetry opposite to that of the light-valve active layer. If we denote the reversal that applies to the optics using a superscript  $^{(\text{MirRev})}$ , we have, in analogy with Equation (7),

$$M^{(\text{MirRev})}[\hat{\theta}] = \begin{pmatrix} m_{11}[-\hat{\theta}] & -m_{21}[\hat{\theta}] \\ -m_{12}[\hat{\theta}] & m_{22}[-\hat{\theta}] \end{pmatrix}, \quad (40a)$$

when

$$M[\hat{\theta}] \equiv \begin{pmatrix} m_{11}[\hat{\theta}] & m_{12}[\hat{\theta}] \\ m_{21}[\hat{\theta}] & m_{22}[\hat{\theta}] \end{pmatrix}. \quad (40b)$$

In Equation (9) we derived the dark-state matrix for a TNLC light valve, but for the moment we consider the general case in which the light valve has matrix elements  $g_{11}, g_{12}, g_{21}, g_{22}$ ; we can alternatively define the general light valve by parameters  $a_1, a_2, a_3, a_4$ , where

$$M_{LV} \equiv \begin{pmatrix} g_{11} & g_{12} \\ g_{21} & g_{22} \end{pmatrix} \equiv a_1 I + a_2 \sigma_x + a_3 \sigma_y + a_4 \sigma_z. \quad (41)$$

with the  $\sigma$  matrices defined in Equation (4). Using Equations (33) and (34), we have

$$M_{\text{Projector}} \equiv \begin{pmatrix} 1 & 0 \\ 0 & 0 \end{pmatrix} \begin{pmatrix} e^{i\Sigma/2} & 0 \\ 0 & e^{i\Sigma/2} \end{pmatrix} \begin{pmatrix} f_{11} & f_{12} \\ f_{11} & f_{12} \end{pmatrix} \begin{pmatrix} e^{i\Sigma/2} & 0 \\ 0 & e^{i\Sigma/2} \end{pmatrix} \begin{pmatrix} 0 & 0 \\ 0 & 1 \end{pmatrix}, \quad (42a)$$

$$\text{where } \begin{pmatrix} f_{11} & f_{12} \\ f_{11} & f_{12} \end{pmatrix} \equiv M_{\text{Perturb}}^{(\text{MirRev})} (a_1 I + a_2 \sigma_x + a_3 \sigma_y + a_4 \sigma_z) M_{\text{Perturb}}. \quad (42b)$$

In obtaining Equation (42) we have made use of the fact that while the  $M_{\text{Rot}}$  component in  $M_{\text{Perturb}}$  [see Equations (31)-(34) above] reverses according to Equation (40), on the collection pass the  $M_{\text{PrePol}}$  factor in  $M_{\text{PBS}}$  will take the form of the leftmost matrix on the right of Equation (40); in this form the polarizer matrix passes bright-state light to the projection lens.

From Equation (42a) we obtain

$$M_{\text{Projector}} = \begin{pmatrix} 0 & f_{12} \\ 0 & 0 \end{pmatrix}. \quad (43)$$

The birefringencelike phase term  $\Sigma$  in the optics [from matrix  $M_{\text{OptPhase}}$  in Equation (30)] thus cancels out in the expression for double-pass propagation through the optics, though it appears implicitly in the elements of  $M_{\text{Perturb}}$ .

We now define  $B$  as the residual dark-state intensity transmitted by the projector. If the efficiencies in the dark state and bright state are equal,  $B$  will be the reciprocal of the contrast ratio. We have, from Equations (37) and (40)-(43),

$$B \equiv |f_{12}|^2 = \left| \left\{ \begin{pmatrix} 1 & -\vec{P}^* \cdot \hat{\theta} \\ \vec{P} \cdot \hat{\theta} & 1 \end{pmatrix} \begin{pmatrix} g_{11} & g_{12} \\ g_{21} & g_{22} \end{pmatrix} \begin{pmatrix} 1 & \vec{P} \cdot \hat{\theta} \\ -\vec{P}^* \cdot \hat{\theta} & 1 \end{pmatrix} \right\}_{12} \right|^2, \quad (44)$$

where  $\{ \}_{12}$  denotes the 1, 2 matrix element. Substituting from Equations (4), (36), and (41),

$$B \equiv |\{ (I + i[\vec{I}\sigma_x - \vec{K}\sigma_y] \cdot \hat{\theta})(a_1 I + a_2 \sigma_x + a_3 \sigma_y + a_4 \sigma_z)(I + i[\vec{I}\sigma_x + \vec{K}\sigma_y] \cdot \hat{\theta}) \}_{12}|^2. \quad (45)$$

Note that the vector quantities in Equation (45) refer to the two-dimensional space of pupil coordinates  $\theta_0, \psi_0$ . The  $x, y, z$  subscripts on the Pauli matrices are standard notation but do not refer to physical coordinates in our application.

Applying the multiplication rules for the Pauli matrices [20] and keeping only first-order terms in  $\hat{\theta}$ , we find

$$B \cong |g_{12} + 2i\hat{\theta} \cdot (a_1 \vec{I} - ia_4 \vec{K})|^2 = |g_{12} + 2i\hat{\theta} \cdot \text{Im}[g_{11}\hat{P}]|^2. \quad (46)$$

According to Equation (46), the off-diagonal element  $g_{12}$  of the light-valve matrix contributes to system background  $B$  via direct depolarization, while the diagonal elements (which determine  $a_1$  and  $a_4$ , and which represent effects such as birefringence) interact with the optics via the rotation and ellipticity parameters  $\vec{K}$  and  $\vec{I}$  to produce contrast loss.

The light-valve matrix  $M_{LV}$  in Equation (9) assumes the specific TNLC form [Equation (6)] for the matrix  $M_{LC}$  of the active layer above the mirror backplane. If we instead allow a more general form for the dark-state matrix of the active layer, which we denote as  $M_{\text{Active}}$  in this more general case, requiring only that  $M_{\text{Active}}$  satisfy the equi-S-P efficient condition of Equation (8), then using  $M_{LV} \equiv -iM_{\text{Active}}^{(\text{rev})}\sigma_z M_{\text{Active}}$  and applying Equation (41), we find

$$\begin{aligned} a_1 &= 2 \sin^2 \mu \sin 2\theta + 2 \cos^2 \mu \sin 2\xi \\ ia_4 &= -2 \sin^2 \mu \cos 2\theta - 2 \cos^2 \mu \cos 2\xi, \end{aligned} \quad (47)$$

where  $\zeta$ ,  $\theta$ , and  $\mu$  are the parameters appearing in the second representation given in Equation (8) (as applied to the active layer), obtaining finally

$$B = g_{12}^2 + 4(\hat{\theta} \cdot \text{Im}[g_{11}\hat{P}])^2$$

$$= g_{12}^2 + 16(\hat{\theta} \cdot [(\sin^2 \mu \sin 2\theta + \cos^2 \mu \sin 2\zeta)\hat{I} + (\sin^2 \mu \cos 2\theta + \cos^2 \mu \cos 2\zeta)\hat{K}])^2. \quad (48)$$

Equation (48) takes  $g_{12}$  to be pure real; this follows from the assumption that  $M_{LV} \equiv -iM_{\text{Active}}^{(\text{rev})}\sigma_z M_{\text{Active}}$ , with  $M_{\text{Active}}$  satisfying Equation (8).

We can also use the third form of Equation (8) to describe the active-layer matrix; expressed in this form, we find

$$B = \frac{4}{(1 + \mathbb{F}'^2 + \mathbb{F}''^2)^2} \{ \frac{1 + \mathbb{F}'^2}{\mathbb{F}''^2 - \mathbb{F}''^2} \sin 2\theta + (\hat{\theta} \cdot [([1 + \mathbb{F}'^2 + \mathbb{F}''^2] \cos 2\theta + [2\mathbb{F}'\mathbb{F}''] \sin 2\theta)\hat{I} + ([1 + \mathbb{F}'^2 - \mathbb{F}''^2] \cos 2\theta - [2\mathbb{F}'\mathbb{F}''] \sin 2\theta)\hat{K})^2 \}, \quad (49)$$

where  $\mathbb{F}'$  and  $\mathbb{F}''$  represent the real and imaginary parts of the depolarization  $\mathbb{F}$  of the central ray at the mirror backplane of the light valve. Equation (49) shows that without the optical system (i.e.,  $\theta \rightarrow 0$ ), contrast loss arises only when the light reaching the mirror backplane has elliptical depolarization (so that the first term  $\mathbb{F}''^2$  in the curly brackets is nonzero); however, when  $\theta \neq 0$ , the optical system interacts with both rotational and elliptical depolarization in the active layer of the light valve to produce contrast loss in the image. A hypothetical ideal light-valve active layer which (in dark state) produced linear polarization at all depths above the mirror backplane (and at all wavelengths) would satisfy  $\mathbb{F}'' = 0$  but would nonetheless show contrast loss in most optical systems of finite NA.

Equations (48) and (49) represent fairly general expressions for the contrast loss along a ray, subject only to the first-order approximation that the total depolarization in the optics is small, and to the approximation that optical elements other than the PBS polarize in phase and not amplitude. Note that Equation (48) involves no complex

parameters [and Equation (49) uses real and imaginary parts explicitly]. The  $g_{12}$  direct depolarization from the light valve makes a contribution to the intensity that is independent of the second term in Equation (48); i.e., the two terms add incoherently. The second term does, however, represent a coherent interaction between the optics and the diagonal matrix elements of the light valve.

We must average Equation (48) over the full cone of rays in the pupil to obtain the actual dark-state background in the projected image. We first introduce the shorthand notation

$$\hat{F} \equiv [F_{\theta}, F_{\psi}] \equiv 2[(\sin^2 \mu \sin 2\theta + \cos^2 \mu \sin 2\zeta) \hat{i} + (\sin^2 \mu \cos 2\theta + \cos^2 \mu \cos 2\zeta) \hat{j}]. \quad (50)$$

The pupil radius is  $NA$ , and we assume the illumination intensity to be uniform over this circular cone; however, to allow for nontelecentricity and misalignment we average Equation (48) over the two-dimensional  $\theta_0, \psi_0$  domain having boundary

$$\sqrt{(\theta_0 - \theta_{\text{Decenter}})^2 + (\psi_0 - \psi_{\text{Decenter}})^2} \leq NA, \quad (51)$$

where  $\theta_{\text{Decenter}}$  and  $\psi_{\text{Decenter}}$  are constants representing the nontelecentricity or misalignment at a particular field location.

Carrying out the average over the circular pupil domain of Equation (51), we find

$$\langle B \rangle_{NA} = g_{12}^2 + (F_{\theta}^2 + F_{\psi}^2) NA^2 + 4(F_{\theta} \theta_{\text{Decenter}} + F_{\psi} \psi_{\text{Decenter}})^2. \quad (52)$$

Equation (52) indicates that contrast loss (essentially

$1/\langle B \rangle$ ) scales quadratically with the angular extents of the beam. The factor of 4 in the third term indicates that contrast loss is fairly sensitive to nontelecentricity in the optics.

### *Particular cases*

We now apply our result from Equation (52) in a number of specific cases.

#### *1. Two-dimensional optical layout; polarizing surfaces tilted about common axis*

Considering for simplicity the telecentric case, if all polarizing surfaces in the optics (including the PBS) are tilted within a common plane (i.e.,

rotation axes for all surface tilts are perpendicular to this plane), Equation (52) becomes

$$\begin{aligned} \langle B \rangle_{NA} &= g_{12}^2 + F_{\theta}^2 NA^2 \\ &= g_{12}^2 + 4([\sin^2 \mu \sin 2\theta + \cos^2 \mu \sin 2\zeta] \mathfrak{S}_{\theta} + [\sin^2 \mu \cos 2\theta + \cos^2 \mu \cos 2\zeta] \mathfrak{M}_{\theta})^2 NA^2. \end{aligned} \quad (53)$$

By definition, the  $\theta$  meridian is always chosen to include the tilt axis of the PBS hypotenuse [i.e., the  $\hat{s}^{(0)}_{\text{PBS}}$  axis about which the PBS hypotenuse is effectively rotated in order to be tilted against the beam], so that  $\theta$  represents the skew angle of the ray against the PBS. In a two-dimensional layout where the tilt axes of all surfaces are parallel, the  $\psi$  coordinate does not affect depolarization. Conversely, in a non-two-dimensional (but telecentric) system where each meridian serves as the skew meridian for at least one surface, Equation (52) indicates that each meridian will make an independent contribution to the dark-state background (assuming, as we have, a uniform circular pupil). Background will often be less when all surfaces are tilted about a common axis, because the  $\psi$  meridian then contributes zero background. However, in the general case the contribution made by each meridian takes the same form, so for brevity we exhibit most of the following results for the case of parallel surface-tilt axes and telecentric optics.

Note that even though the  $\theta$  and  $\psi$  ray components make independent contributions to the intensity background of Equation (52), it should not be concluded that optical surfaces tilted in one meridian have effects independent of those of surfaces tilted in the other. In general, an optical surface which is tilted in one meridian will still make a contribution to the parameters  $\mathfrak{S}$  and  $\mathfrak{M}$  for the other meridian, except in the particular case where all surfaces are tilted about parallel tilt axes; in this special case we have seen that  $\mathfrak{S}_{\psi}$  and  $\mathfrak{M}_{\psi}$  vanish, as in Equation (53). In general, Equation (19) shows that once a ray has become depolarized, succeeding surfaces usually introduce additional changes in polarization even when the ray has no skew incidence component.

## 2. Light valve has mirrorlike dark state

In this case  $\mu = 0$  and  $\zeta = \pi/2$  in Equation (8), and Equation (53) becomes

$$\langle B \rangle_{NA} = g_{12}^2 + \mathfrak{M}_{\theta}^2 NA^2, \quad (54)$$

where for simplicity we have assumed telecentric optics in which the tilt axes for all polarizing coatings are parallel. Parameter  $\mathfrak{S}$  does not appear



in Equation (54), showing that skew-ray ellipticity introduced by the optics will cancel out in double pass if the light valve is mirrorlike; i.e., elliptical depolarization in the optics will not cause dark-state background. Recall that in our first-order treatment we expand the depolarization against axes corresponding to the central ray, denoted by a superscript  $(0)$ . [An exception was made to this approach in Equation (21).] The rotation  $\Omega$  of concern in Equation (54) is thus a rotation relative to the plane of incidence (at tilted coatings) of the central ray, evaluated when the ray illuminates the light valve. This is illustrated in **Figure 8**, which shows schematically the polarization ellipse of a skew ray illuminating a light valve in an optical system with two tilted coatings. In the figure the ray reflects from two tilted surfaces which are hypotenuse surfaces in the two cube elements. Once the incident ray reflects from the second hypotenuse coating, it is traveling out of the perspective diagram toward the viewer; it then illuminates a light valve on the front surface of the bottom cube. The figure shows the case in which the optical system introduces ellipticity but not rotation. The major axis of the skew ray's ellipse is therefore aligned with the plane of the central ray. (The central ray is shown in green.) Because of this alignment the folded path of the central ray then forms a plane of symmetry for the electric field as well as for the rays. Equation (54) shows that because of this symmetry the depolarization is canceled out in the return pass through the optics.



Figure 8

On the other hand, rotational depolarization doubles in amplitude in the round trip [i.e., quadruples in intensity; the resulting factor of 4 is canceled in Equation (54) when  $\theta$  is averaged over the pupil]. Of course, the actual polarization state of the round-trip light is determined by the pass direction of the PBS at the exit face; the implication of Equation (54) is that, when the single-pass depolarization is purely rotational, the dark-state intensity measured in double pass will be four times larger than the intensity measured in single pass between crossed polarizers.

### 3. Light valve is "ideal"

A dark-state light valve can be considered nominally ideal if its reflectivity between crossed polarizers is zero. An ideal light valve is not necessarily mirrorlike in the dark state; the requirement that its off-diagonal elements be zero means that when the matrix for the active layer of the light valve is expressed in the third form of Equation (8), parameter  $\mathbf{F}$ , must be pure real. A light valve that is ideal in this sense will not necessarily have zero dark-state intensity when used in an optical system. Considering for simplicity the case of a telecentric system with a two-dimensional layout, Equations (49) and (52) become

$$\langle B \rangle_{NA} = NA^2 [\mathfrak{R}_\theta \sin 2\mathfrak{A} + \mathfrak{I}_\theta \cos 2\mathfrak{A}]^2. \quad (55)$$

An ideal light valve must have a dark state that is essentially equivalent to a retarder placed over a mirror (with the retarder axes aligned with the polarization of the illuminating central ray). If the equivalent retarder for such an ideal light valve is quarter-wave,  $2\mathfrak{A} = 90^\circ$ , and the dark-state intensity will be zero in an optical system that induces no ellipticity in the illumination. On the other hand, if the light valve is equivalent to a mirror (case 2 above), the dark-state intensity will be zero if the optics do not induce rotation. In general, the dark-state intensity of the ideal light valve will be zero in an optical system if  $\text{Re}[e^{-2j\mathfrak{A}} \hat{\mathbf{p}} \cdot \hat{\boldsymbol{\theta}}] = 0$ . In this case the depolarization  $\delta E/E$  at the mirror backplane of the light valve can have a constant rotation  $\text{Re}[\mathfrak{F},]$  that is common to all rays; the remaining ray-dependent portion of the polarization must be purely elliptical. This represents a generalization of the symmetry condition in [Figure 8](#) to the case of any ideal light valve (not necessarily mirrorlike).

#### 4. Light valve is nearly ideal

The crossed-polarizer reflectivity of a dark-state light valve must be small compared to 1 if the light valve is to provide useful performance. For such a light valve we can show that one portion of the single-pass depolarization from the optics will cancel in double pass, while the remaining portion (in quadrature with the first) will double. For a mirrorlike dark state (case 2 above) these portions are, respectively, the ellipticity and rotation, but in general they are defined by a phase relationship involving the light-valve depolarization. The light-valve depolarization also contributes a direct term to the dark state. To derive these results, we rewrite Equation (48) as

$$B = g_{12}^2 \left\{ \frac{1}{4} + \left( \hat{\boldsymbol{\theta}} \cdot \begin{bmatrix} g_{11} \\ - \\ g_{12} \end{bmatrix} \right)^2 \right\}, \quad (56)$$

where we have made use of the fact that  $g_{12}$  is pure real if the active layer of the light valve obeys Equation (8). The quantity  $g_{11}/g_{12}$  appearing in Equation (56) can be rewritten as  $1/D^*$ , where  $D$  is the depolarization introduced by the light valve alone; i.e.,  $D$  is the ratio  $E_x/E_z$  when reflected field  $\hat{\mathbf{E}}_{\text{Reflected}} = (E_x, E_z)$  is produced by illuminating the light valve (at  $\hat{\boldsymbol{\theta}} = 0$ ) with a unit amplitude polarized along  $\hat{\mathbf{z}}$ . If the light valve provides high contrast,  $g_{11}$  will have magnitude close to 1, and to first order we can set  $D = g_{12} e^{j\Lambda_{LV}}$ , where  $\Lambda_{LV}$  is the phase of the light-valve depolarization and  $g_{12}$  its magnitude. (Since  $g_{12}$  is real, it does not affect

the phase of  $D$ ;  $-\Lambda_{LV}$  is the phase of  $g_{11}$ .) In the general case where light-valve contrast is not necessarily high, we can set  $|g_{11}|^2 = 1 - g_{12}^2$ . The single-pass transmission of the optics between crossed polarizers (integrated over  $NA$ ) is  $\langle B_{\text{One-pass}} \rangle = |P|^2 NA^2 / 4$ . Defining  $\Lambda_{\text{Optics}}$  as the phase of the optics depolarization  $P$ , we then have for the double-pass output between crossed polarizers [integrating Equation (56) over the pupil],

$$\begin{aligned} \langle B \rangle &= B_{LV} + 4 \langle B_{\text{One-pass}} \rangle (1 - B_{LV}) \sin^2 (\Lambda_{LV} + \Lambda_{\text{Optics}}) \\ &\cong B_{LV} + 4 \langle B_{\text{One-pass}} \rangle \sin^2 (\Lambda_{LV} + \Lambda_{\text{Optics}}), \end{aligned} \quad (57)$$

where we have denoted the dark-state reflectivity  $g_{12}^2$  of the light valve alone as  $B_{LV}$ , and where for simplicity we have assumed telecentric optics, with surface tilts about parallel axes. The upper form of Equation (57) applies in general; the lower form, when the light-valve contrast is large compared to 1. Equation (57) states that when a light valve has reasonably high contrast, part of the single-pass depolarization introduced by the optics will double in the return pass, namely the depolarization that is in quadrature with the depolarization from the light valve. The doubled amplitude causes a fourfold increase in dark-state intensity, as indicated in Equation (57). The remaining portion of the optics depolarization [of squared magnitude  $\langle B_{\text{One-pass}} \rangle \cos^2 (\Lambda_{LV} + \Lambda_{\text{Optics}})$ ] is automatically canceled in double pass. The quadrature relationship is a consequence of the opposite reversal symmetries obeyed by the optics and the active layer of the light valve.

##### 5. Twisted nematic liquid crystal light valve

Using Equation (9) to calculate  $a_1$  and  $a_4$  in Equations (41) and (49) [or, alternatively, solving for the parameters in Equation (8)], we find

$$\begin{aligned} \langle B \rangle &= \left( \frac{2\alpha\beta \sin^2 \gamma}{\gamma^2} \right)^2 + \left( \Im_{\theta} \left[ 1 - \frac{2\beta^2 \sin^2 \gamma}{\gamma^2} \right] \right. \\ &\quad \left. + \Im_{\theta} \left[ \frac{\beta \sin (2\gamma)}{\gamma} \right] \right)^2 NA^2 + B_{0,LV} + B_{0,\text{Optics}}, \end{aligned} \quad (58)$$

where again to shorten the result we have assumed telecentricity and a common tilt axis.

Since Equation (58) represents a case of considerable practical interest, we have added two phenomenological parameters  $B_{0,LV}$  and  $B_{0,Optics}$  that account for any background contributed by mechanisms outside the models of Equations (9) and (19). ( $B_{0,LV}$  refers to such residual background from the light valve,  $B_{0,Optics}$  to that from the optics.) The first term in Equation (58) represents the direct depolarization contribution from the light valve; the light valve also interacts with rotation  $\Re$  and ellipticity  $\Im$  in the optics via the two terms in square brackets, which then contribute to background  $\propto NA^2$ .

**Figure 9** shows a plot of the three TNLC factors appearing in Equation (58); the  $g_{12}$  off-diagonal term, and the two expressions in square brackets which multiply the rotation and ellipticity contributed by the optics.

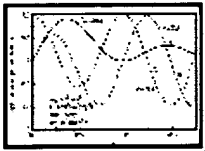


Figure 9

#### 6. Twisted nematic liquid crystal light valve operating in near-mirror condition

The Jones matrix for the single-pass TN active layer [Equation (6)] reduces to the identity matrix when parameter  $\beta$  (defined by  $\beta \equiv \pi D(n_e - n_o)/\lambda$ ) takes on the value  $\sqrt{m^2\pi^2 - \alpha^2}$ , with  $\alpha$  the twist angle and  $m$  a positive integer. The light-valve matrix [Equation (9)] then becomes equivalent to a mirror, and dark-state background is given by  $(\Re_\theta^2 + \Im_\psi^2)NA^2$ . We would typically expect this condition to be met at only one wavelength in the spectral illumination band. Taking as an example  $\alpha = 45^\circ$ ,  $m = 1$ , we can expand Equation (58) in a small departure  $\delta\beta$  from the point of mirrorlike behavior (so that  $\beta \equiv \beta - \sqrt{15}\pi/4$ ), to obtain

$$\begin{aligned} \langle B \rangle \cong & \left( \frac{15\sqrt{15}\delta\beta^2}{128} \right)^2 + NA^2 \left[ \Re_\theta + \Im_\theta \frac{15}{8} \delta\beta \right. \\ & \left. + \left( \frac{3\sqrt{15}}{64\pi} \Im_\theta - \frac{225}{128} \Re_\theta \right) \delta\beta^2 + \dots \right]^2 + B_{0,Optics} + B_{0,SLM}. \end{aligned} \quad (59)$$

If  $NA$  and  $\delta\beta$  are regarded as first-order quantities, then in lowest order the light valve interacts with the optics in mirrorlike fashion, via the quadratic  $\Re^2 NA^2$  term. If rotation  $\Re$  and ellipticity  $\Im$  are both nonzero, the next-

order term is cubic, proportional to  $NA^2\beta$  and to  $\mathfrak{N} \times \mathfrak{S}$ . When rotation is zero, the two lowest-order terms are both quartic, proportional to  $NA^2\beta^2$  and to  $\beta^4$ . Note that unless  $\mathfrak{N} = 0$ , the quadratic and cubic terms involving the optics tend to dominate the  $g_{12}$  term that arises from the light valve alone. Unless NA can be regarded as negligible, or the optical system introduces no rotation, there can be a fairly substantial range of wavelengths about  $\beta = 0$  in which depolarization involving the optics dominates over the contrast measured from the light valve alone.

### 7. PBS/TNLC module

The most common optical arrangement for reflective light valves is the simple PBS. Light of a particular color is introduced into one port of the beam splitter where it illuminates the light valve (e.g., in reflection, as in [Figure 3](#)); light switched to the bright state exits the PBS through a different port. Bleha [27] has published a typical layout. Multiple modules can be used to project different colors, or the colors can be projected sequentially from a single module at a high enough switching speed to appear continuous. Alternatively, a mosaic of (normal-incidence) color filters can be placed on the pixel grid. The common feature in all such approaches is that no tilted coatings other than the PBS hypotenuse see both bright-state and dark-state light.

In such a system  $\mathfrak{S}_\theta = 0$  (along with  $\mathfrak{S}_\psi, \mathfrak{N}_\psi$ ), and  $\mathfrak{N}_\theta = 1/(n_{\text{PBS}} \tan \phi)$ , where  $\phi$  is the angle of incidence at the PBS ( $\phi = 45^\circ$  for a cube beam splitter) and  $n_{\text{PBS}}$  is the refractive index of the PBS substrates. The illumination polarization is rotated but not elliptical. For a TNLC light valve, Equation (58) becomes

$$\begin{aligned} \langle B \rangle_{\text{NA}} = & \left( \frac{2\alpha\beta \sin^2 \gamma}{\gamma^2} \right)^2 \\ & + \left( \frac{1}{\gamma^2} \frac{2\beta^2 \sin^2 \gamma}{\gamma^2} \right)^2 \frac{NA^2}{n_{\text{PBS}}^2 \tan^2 \phi} + \frac{B_{0,\text{LV}} + B_{0,\text{Optics}}}{B_{0,\text{Optics}}} \end{aligned} \quad (60)$$

If the PBS coating is of the usual MacNeille type, the parameters  $n_{\text{PBS}}$  and  $\phi$  are not fully independent, because light must be incident at the interfaces between the low- and high-index layers at the Brewster angle. If we make such Brewster incidence an explicit condition, Equation (60) can be rewritten in various forms:

$$\begin{aligned}
\langle B \rangle_{NA} \cong & \left( \frac{2\alpha\beta \sin^2 \gamma}{\gamma^2} \right)^2 \\
& + \left( 1 - \frac{2\beta^2 \sin^2 \gamma}{\gamma^2} \right)^2 \left[ \frac{1}{n_L^2} + \frac{1}{n_H^2} - \frac{1}{n_{PBS}^2} \right] NA^2 + B_{0,LV} + B_{0,Optics}. \quad (61)
\end{aligned}$$

or

$$\begin{aligned}
\langle B \rangle_{NA} \cong & \left( \frac{2\alpha\beta \sin^2 \gamma}{\gamma^2} \right)^2 \\
& + \left( 1 - \frac{2\beta^2 \sin^2 \gamma}{\gamma^2} \right)^2 \left[ \frac{1}{n_L^2} + \frac{1}{n_H^2} \right] \cos^2 \phi NA^2 + B_{0,LV} + B_{0,Optics}. \quad (62)
\end{aligned}$$

where  $n_L$  and  $n_H$  are the indices of the low- and high-index materials in the PBS coating.

#### 8. PBS/TNLC module with quarter-wave retarder

We have seen in item 2 above that when the light valve is mirrorlike, ellipticity in the illumination will be canceled out in double pass through the optics; two-pass depolarization arises only from rotation in the illuminating polarization. When the illumination depolarization is pure rotation, as with the PBS/TNLC module in item 7 above, it can be converted to purely elliptical depolarization by placing a quarter-wave retarder on top of the light valve. The waveplate must in the ideal case be oriented so that its retardation axes are rectilinear with the illuminating dark-state polarization of the central ray. The TNLC is likely to be mirrorlike at only a single wavelength in the band; when we apply Equation (58) in the case of pure ellipticity from a PBS and 90° retarder, we find that for other wavelengths,

$$\langle B \rangle_{NA} = \left( \frac{2\alpha\beta \sin^2 \gamma}{\gamma^2} \right)^2 + \beta \sin^2 (2\gamma) NA^2$$

$$+ \left( \frac{\gamma}{\gamma^2} \right) \frac{+ B_{0,LV} + B_{0,Optics}}{n_{PBS}^2 \tan^2 \Phi} \quad (63)$$

The difference between Equation (60) and Equation (63) is in the two LC factors that multiply the optics factor  $NA^2/(n_{PBS}^2 \tan^2 \Phi)$ . These are two of the curves plotted in [Figure 9](#); without the waveplate, the interaction depolarization is largest in the center of the band, whereas with the waveplate, contrast loss is eliminated at the center of the band (where the light valve is mirrorlike). At other wavelengths the dark-state background with the quarter-wave retarder remains larger than the  $g_{12}^2$  term contributed by the light valve alone. Even with the waveplate in place, the quadratic interaction term is still the dominant source of contrast loss near the center of the band, where the light-valve term is quartic in  $\Delta\lambda$ . (Of course, all contrast losses are small in this regime.) It should also be noted that Equation (63) assumes an achromatic quarter-wave plate; the dispersion that would be present in a simple single-layer retarder is neglected for simplicity.

#### 9. Light valve rotated under polarizing microscope

The field of view in a microscope is small enough that in a reflection-mode instrument designed for polarization work, the beam can be expanded through the beam splitter in an almost collimated condition; then  $NA$  is  $\sim 0$  and compound-angle effects are avoided. The intensity measured between crossed polarizers in such an instrument is simply  $g_{12}^2$ . In a sense, Equation (52) is a generalization of this simple result to include compound-angle effects at finite  $NA$ , but we can generalize it in another way, by calculating residual dark-state intensity as a function of light-valve orientation. [Of course, Equation (52) also applies to a rotated light valve if the active layer is modified by a rotation matrix.]

As in the case of Equation (52), we impose only one constraint on the light-valve matrix  $[(g_{11}, g_{12}), (g_{21}, g_{22})]$ , namely that it arise from a nonabsorbing active layer (or a layer with equal absorption in the two polarizations) placed above a mirror backplane. Such an active layer must satisfy Equation (8) above; if in its nominal orientation ( $\theta = 0$ ) the active layer matrix is parametrized according to the second form in Equation (8), then we find using rotation matrices and some algebra that the reflectance measured between crossed polarizers when the active layer is rotated to a new orientation  $\theta$  is given by

$$R(\theta) = R_0 \cos^2 [2(\theta - \theta_0)] + B_{0,LV} = R_0 \sin^2 [2 \quad (64)$$

$$\theta'] + B_{0,LV},$$

where  $B_{0,LV}$  is the same parameter that appears in Equation (58), and where

$$R_0 = 1 - (\sin^2 \mu \cos 2\theta + \cos^2 \mu 2\xi)^2, \quad (65)$$

and

$$\tan 2\theta_0 = \frac{\cos(\theta + \xi)}{\tan 2\mu} - \frac{\sin(\theta + \xi)}{\tan(\theta - \xi) \sin 2\mu}, \quad (66)$$

and where  $\theta' \equiv \theta - [\theta_0 - (2m + 1)\pi/4]$ , with  $m$  an integer.

According to Equation (64), the observation of a harmonic intensity variation (having  $90^\circ$  period) when a reflective light valve is rotated between crossed polarizers is generic, and in itself conveys little information about the properties of the light valve; however, quantitative measurements of the angle of maximum reflectivity  $\theta_0$  and the maximum reflectivity value  $R_0$  suffice to constrain the active layer in two of the three degrees of freedom permitted by Equation (8). The  $\cos^2(2\theta)$  modulation will be zero in all orientations only if  $R_0 = 0$  (in which case it follows from Equations (8) and (65) that the active layer must be either null, equivalent to a half-wave retarder, or equivalent to a pure rotation (optically active layer), but in the ideal case where  $B_{0,LV} = 0$ , the reflectance between crossed polarizers will always have a zero at  $\theta = \theta_0 + \pi/4$ . Because  $\theta = 0$  corresponds to the normal orientation of the light valve, it may be convenient to shift the angular coordinate system according to the lower form of Equation (64), since contrast is likely to be high at small values of  $\theta$ .

#### 10. TNLC light valve rotated under polarizing microscope

In the particular case of a TNLC light valve [as in Equation (9), single-pass active layer as in Equation (6)],

Equation (64) becomes

$$R(\theta) = R_0 \sin^2 [2(\theta - \theta'_0)] + B_{0,LV}, \quad (67)$$



$$R_0 = \left( \frac{2\beta \sin \gamma}{\gamma} \right)^2 \left( 1 - \left[ \frac{\beta \sin \gamma}{\gamma} \right]^2 \right)$$

and

$$\tan 2\theta'_0 = \frac{\alpha \tan \gamma}{\gamma} \quad (68)$$

## Discussion

We now discuss some implications of the results of the previous section. **Figure 10** plots Equation (64) (at  $\theta = 0$ ) as a function of  $\lambda$ , for a TNLC active layer [Equations (67) and (68)], using  $\Delta n[\lambda]$  values for a commercially available liquid crystal material. The parameter  $\alpha$  is set to  $\pi/4$ . The curve of **Figure 10** is the spectral response of the light valve if measured between crossed polarizers using a polarizing microscope (see also below). **Figure 10** can also be regarded as an application of the curve of **Figure 6** to a particular LC layer. The LC thickness is chosen such that when temperature  $T = 30^\circ\text{C}$ , parameter  $\gamma$  becomes equal to  $\pi$  at  $\lambda = 545$  nm; 545 nm is then the nominal wavelength of maximum contrast.  $\Delta n \equiv n_e - n_o$  is about 0.2 at this wavelength, and the required LC thickness is 2.64  $\mu\text{m}$ .  $\lambda = 545$  nm might, for example, be the center of a green channel extending from 515 nm to 575 nm. For the sake of illustration we have set  $B_{0,LV} = 0.002$ . The change in  $n_e - n_o$  with temperature is roughly -0.35% per  $^\circ\text{C}$ . (A slightly more detailed  $T$  dependence is used in the plots.) The spectral dispersion in  $n_e - n_o$  is roughly -0.5% per 1% increase in  $\lambda$ .



Figure 10

All curves in **Figure 10** are essentially equivalent to the curve in **Figure 6**, with a different mapping of parameter  $\beta$  onto  $\lambda$  for each temperature. Since  $\beta \equiv \pi (n_e - n_o)d/\lambda$ , a pair of balancing shifts  $\Delta T$  and  $\Delta \lambda$  that hold  $\beta$  at some constant value (e.g., the value  $(\sqrt{15}/4)\pi$  associated with the minimum of the curve) must be related by

$$\frac{1}{\Delta\lambda} \frac{\partial \beta}{\partial T} \frac{\partial (\ln [\Delta n])}{\partial T} \approx \frac{1}{\lambda_0 \Delta T} \frac{\partial \beta}{\partial \lambda} \frac{\partial (\ln [\Delta n / \lambda])}{\partial (\ln \lambda)}. \quad (69)$$

If  $\Delta n$  changes by 0.35% per °C, and  $\Delta n / \lambda$  by 1.5% per 1% change in  $\lambda$ , then Equation (69) predicts a 0.23% shift in minimum wavelength per °C. The curves of [Figure 10](#) shift with temperature at about this rate. At a fixed 30°C temperature, the range of wavelengths where background is below 0.01 is 115 nm; however, it is only over a smaller 85-nm-wavelength range that background is below 0.01 at all temperatures between 20°C and 40°C. A 30-nm contraction of the tolerance window over 20°C at  $\lambda = 545$  nm is approximately what would be expected from the linear approximation in Equation (69).

We next consider the effect of the optical system. **Figure 11** plots the system background when the light valve of [Figure 10](#) is used with a basic PBS/TNLC module [Equation (60)]. The calculation uses  $n_{\text{PBS}} = 1.85$  and  $NA = 0.143$  (f/3.5 optics). **Figure 12** plots the example of [Figure 10](#) with a quarter-wave retarder placed over the TNLC light valve [Equation (63)], also for the case  $n_{\text{PBS}} = 1.85$  and  $NA = 0.143$ . In both cases a constant scatter background from the optics  $B_{0,\text{Optics}} = 0.002$  is assumed for purposes of illustration. Over small changes in temperature and wavelength, the dark-state intensity in [Figure 11](#) is dominated by the constant  $n^2 NA^2$  background that the PBS would produce if the light valve were perfectly mirrorlike. When a quarter-wave retarder is added, as in [Figure 12](#), the background level at fixed  $NA$  has a quadratic variation with wavelength over much of the plotted region.

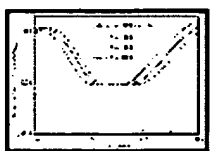


Figure 11

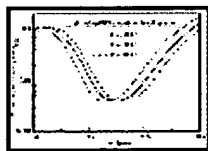


Figure 12

[Figures 11](#) and [12](#) are essentially plots of (contrast)-1 versus wavelength for a TNLC light valve whose dark state is mirrorlike at  $\lambda = 545$  nm. (Strictly speaking, contrast can be identified as the reciprocal of  $\langle B \rangle$  only if dark-state and bright-state efficiencies are equal.) **Figures 13** and **14** show integrals over a spectral range  $\Delta\lambda = 60$  nm of the curves of [Figures 11](#) and [12](#); the horizontal axis in [Figures 13](#) and [14](#) is the center wavelength  $\lambda_0$  of the integration band. In a sense, [Figures 13](#) and [14](#) could be regarded as plots of integrated contrast in a color channel having 60-nm bandwidth. These integrations are somewhat artificial, because the mean wavelength of the color channel is shifted without regard for chromaticity requirements, but the curves of [Figures 13](#) and [14](#) are roughly

equivalent to plots of  $\lambda$ -averaged background as a function of LC thickness  $d$ , if due allowance is made for the dispersion of  $\Delta n$ . The finite-wavelength band always degrades contrast slightly in the region of interest; the degradation can be regarded as a larger relative effect in the case of Figure 14 with quarter-wave retarders, because the total background is lower.

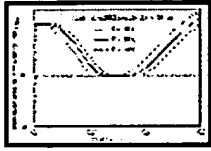


Figure 13



Figure 14

The analysis of the preceding sections allows contrast to be calculated for a particular optical system of interest, but there are general trends that can be noted if further simplifications are made. First, if we regard the NA, the relative bandwidth  $\Delta\lambda/\lambda_0$ , and the fractional cell-gap error  $\Delta d/d$  (including the effective change in cell gap due to temperature excursion) as first-order quantities, then Equation (59) above shows that the lowest-order background term arises from rotation in the illuminating polarization (causing background  $B \sim \pi^2 NA^2$ ). For the PBS/TNLC module without quarter-wave plates, we can therefore say as a rough approximation that, for  $\Delta\lambda/\lambda_0$  and  $\Delta d/d$  small, background is approximately

$$B \approx B_{0,LV} + \frac{NA^2}{B_{0,Optics} + \frac{n_{PBS}^2}{\tan^2 \phi}}. \quad (70)$$

If  $\phi = 45^\circ$  and  $n_{PBS} \cong 1.7$ , we then have as a rough scaling rule

$$B \sim B_{0,LV} + \frac{NA^2}{B_{0,Optics} + 3}. \quad (71)$$

Equation (71) is highly simplified, but it suggests that a

typical requirement of contrast  $\geq 100:1$  limits NA to  $\sim 0.15$  for a PBS/TNLC module operating without quarter-wave retarder.

The case in which a quarter-wave retarder is added to the module (item 8 above) is somewhat more complicated. An expansion along the lines of Equation (59) contains a number of lowest-order (quartic) terms; the

essential action of the retarder is in effect to subtract the lowest-order (quadratic) term represented by Equation (70). The fully general expression in Equation (63) is fairly simple, but becomes more complicated when expressed in terms of the underlying physical parameters  $d$ ,  $\Delta n(\lambda, T)$ , and  $\lambda$ . To obtain a simplified result, we expand  $\beta$  in terms of a small shift  $\delta\lambda$  away from the central wavelength  $\lambda_0$ , a small temperature excursion  $\Delta T$ , and a small departure  $\Delta d$  of LC thickness from nominal:

$$\frac{\beta[\lambda+\delta\lambda]}{\sqrt{1-W^2}} \cong \pi \left( \frac{1}{K} + \frac{\delta\lambda}{\lambda_0} + \frac{\delta\beta_0}{\beta_0} \right), \quad (72)$$

where

$$K \equiv \frac{\partial \ln \left( \frac{\Delta n(\lambda, T)}{\lambda} \right)}{\partial \ln \lambda} \bigg|_{\lambda=\lambda_0}. \quad (73)$$

Parameter  $W$  is defined by  $W \equiv \alpha/\pi$ , and the systematic fractional offset in  $\beta$  is defined by

$$\frac{\delta\beta_0}{\beta_0} \equiv \frac{\Delta d}{d} + \Delta T \frac{\partial \ln(\Delta n)}{\partial T}. \quad (74)$$

We approximate Equation (63) under the assumption that the background intensity of interest is the average of  $B$  over all wavelengths present in a particular color channel (as well as over NA); the spectral extent  $\Delta\lambda$  of the color channel is defined by  $\lambda_0 - (\Delta\lambda/2) \leq \lambda_0 + \delta\lambda \leq \lambda_0 + (\Delta\lambda/2)$ . We would like to estimate the integrated channel background as a function of channel bandwidth  $\Delta\lambda$ , LC error  $\delta\beta_0/\beta_0$ , and NA. In general the channel spectrum has some distribution  $P(\lambda)$ , which may include a lumen-weighting factor representing the eye's efficiency. For a flat spectrum [i.e.,  $P(\lambda) = 1$ ], the average over the  $m$ th power in a spectral expansion is given by

$$\left\langle \left( \frac{\delta\lambda}{\lambda_0} \right)^m \right\rangle_\lambda = \frac{1}{\lambda_0^m} \frac{\int_{-\Delta\lambda/2}^{+\Delta\lambda/2} (\delta\lambda)^m d\lambda}{\int_{-\Delta\lambda/2}^{+\Delta\lambda/2} d\lambda} \quad (75)$$

$$= \begin{cases} \frac{1}{2^m(m+1)} \left( \frac{\Delta\lambda}{\lambda_0} \right)^m & m \text{ even,} \\ 0 & m \text{ odd.} \end{cases}$$

For  $m = 2$ , the flat spectrum average of  $(\delta\lambda/\lambda)^2$  from

Equation (75) is  $(1/12)(\Delta\lambda/\lambda)^2$ , where  $\Delta\lambda$  is the full width of the channel. For the more general case where  $P(\lambda)$  is not constant, we then define an effective channel width  $(\Delta\lambda/\lambda_0)_{\text{eff}}$  according to

$$\left( \frac{\Delta\lambda}{\lambda_0} \right)_{\text{eff}} \equiv \frac{1}{\lambda_0} \sqrt{12 \frac{\int_{-\Delta\lambda/2}^{+\Delta\lambda/2} P(\lambda_0 + \delta\lambda) (\delta\lambda)^2 d\lambda}{\int_{-\Delta\lambda/2}^{+\Delta\lambda/2} P(\lambda_0 + \delta\lambda) d\lambda}}. \quad (76)$$

For simplicity we further assume that the average of  $(\delta\lambda/\lambda)^4$  is equal to  $(1/80)(\Delta\lambda/\lambda_0)^4_{\text{eff}}$ , even though according to Equation (75) this is only strictly true for a flat spectrum. We similarly make the approximation that the average of any odd power of  $(\delta\lambda/\lambda)$  is negligible, even with a nonconstant spectrum. Dispersion in the retarder is also neglected.

Keeping only the lowest-order terms in Equation (63), we find

$$\begin{aligned} \frac{\langle B \rangle_{\lambda, NA}}{W^2)^3} &\approx \pi^2 (1 - \left\{ \frac{\pi^2 W^2 (1 - \left[ \frac{K^4}{80} \left( \frac{\Delta\lambda}{\lambda_{\text{eff}}} \right)^4 + \frac{K^2}{2} \left( \frac{\Delta\lambda}{\lambda_{\text{eff}}} \right)^2 \left( \frac{\beta_0^3}{\beta_0} \right)^2 + \left( \frac{\beta_0^3}{\beta_0} \right)^4 \right]}{W^2)^2} \right\} \\ &+ \frac{NA^2}{K^2} \frac{\Delta\lambda^2}{\beta_0^2} + \frac{\beta_0^3}{\beta_0^2} + B_{0,LV} + B_{0,Optics} \end{aligned} \quad (77)$$

$$n_{\text{PBS}}^2 \tan^2 \Phi \left| 12 \left( \lambda \right)_{\text{eff}} \left( \beta_0 \right) \right| \left\{ \right.$$

The coefficients in Equation (77) that multiply powers of the systematic error ( $\delta\beta/\beta$ ) tend to be somewhat larger than those multiplying powers of the bandwidth  $(\Delta\lambda/\lambda)_{\text{eff}}$ . Image brightness increases as spectral bandwidth increases, but chromaticity considerations prevent bandwidth  $(\Delta\lambda/\lambda)_{\text{eff}}$  from exceeding  $\sim 0.12$  to  $0.18$  in a single color channel. Image brightness also increases with increasing NA; however, besides lowering contrast, practical considerations such as lens cost and component size also limit NA in this type of projector.

To simplify Equation (77) still further, we assume that at the practical limit,  $NA \sim 0.25$  and  $(\Delta\lambda/\lambda)_{\text{eff}} \sim 0.15$ . For  $K \sim 1.5$  and  $W = 0.25$ , we find from Equation (77) that the quartic terms in cell-gap error are fairly small, and that

$$\langle B \rangle_{\lambda, NA} \sim B_{0, LV} + B_{0, \text{Optics}} + 0.0035 + \left( \frac{\delta\beta_0}{\beta_0} \right)^2. \quad (78)$$

Equation (78) is of course very rough, but it suggests that when a quarter-wave retarder is combined with a PBS/TNLC module in a projector with  $\sim 100:1$  contrast target, compound-angle depolarization will not be the dominant factor limiting the NA as long as cell-gap errors (and equivalent temperature excursions) are held to  $\sim 5\%$ . When we consider depolarization from the light valve alone, we obtain tolerances that are  $\sim 50\%$  more relaxed. **Figure 15** shows the result of integrating with respect to  $\lambda$  the curve of [Figure 10](#) for the background contribution of the light valve alone; the range of integration is the same as in [Figures 13](#) and [14](#). Comparison of [Figures 13](#), [14](#), and [15](#) illustrates the narrowing of light-valve LC thickness tolerances due to interaction with the optical system.

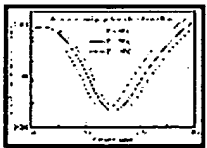


Figure 15

The incoherent contribution from the optics,  $B_{0, \text{Optics}}$ , can be measured by replacing the light valve in the PBS/TNLC module with a mirror (leaving the quarter-wave retarder in place). Because of the interaction term in Equation (63), it is not accurate to calculate system contrast by simply adding to  $B_{0, \text{Optics}}$  the contribution of the light valve as measured with a

polarizing microscope. Instead, more extensive light-valve measurements must be made in order to determine the thickness  $d$  of the LC active layer as fabricated (including possible thickness variation over the active area), and the incoherent background term  $B_{0,LV}$ . We have described our measurement procedure and apparatus elsewhere [28, 29]. **Figure 16** illustrates one complication that is seen in experimental data. The solid curve shows measured reflectivity as a function of  $\lambda$  for a TNLC light valve between crossed polarizers, at  $NA = 0.2$ . The ripple structure is due to interference across the TNLC layer. Yang and Takano have analyzed this phenomenon in detail as a multiray Fabry-Perot interference across a dispersive TN medium [30]. The dashed curves in **Figure 16** are fittings of Equations (67) and (68) to the spectrum, which we use to determine the LC thickness  $d$ . We obtain reasonably consistent results with this method, even though Equation (67) neglects multiple reflections within the LC layer.

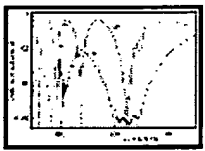


Figure 16

## Summary

Projectors that use reflective light valves must employ beam splitters or analogous components to separate bright-state light from dark-state light. With transmissive light valves, this function can be carried out by a simple sheet post-polarizer which trims dark-state light from the bright-state image beam. However, when the light valve is reflective, both states must be allowed to propagate in the space above the substrate, and the beam-splitter element (PBS) must actually separate the two beams.

Beam-dividing interference coatings give rise to polarization crosstalk via compound-angle depolarization, as illustrated in **Figure 3** for a PBS coating. Other tilted coatings in the projection optics may also contribute to this depolarization, as illustrated in **Figure 4**. The depolarization gives rise to undesired intensity in the dark-stage image, causing contrast to degrade proportional to  $NA^{-2}$ . The unwanted background has the same polarization as the bright-state image and cannot be filtered out with a supplementary polarizer.

In Equations (19)-(22) we have presented a solution for the depolarization arising in a general optical system, retaining terms in the depolarization amplitude proportional to  $NA$  ( $\propto NA^2$  in intensity). Good agreement has been found with exact numerical polarization ray tracing [using Equations (10) and (11)] when  $NA \lesssim 0.14$  (i.e., for apertures below  $\sim f/3.5$ ). Our solution applies to any assembly of tilted coatings, so long as 1) all surfaces are tilted in such a way that the polarization of the central ray is either pure S or pure P (i.e., the optical system introduces no deliberate

depolarization), and 2) none of the tilted optical coatings through which the beam passes in transmission are deposited on tilted refractive wedges (which if used would cause severe aberration of the beam). The solution applies to systems employing tilted-plane parallel substrates (such as plate dichroic filters or plane parallel tilted air spaces), as well as TIR reflections or tilted internal coatings like that in a PBS cube.

We have reviewed the Jones-matrix theory of reflective twisted nematic liquid crystal (TNLC) light valves, and have noted that the dark state in such light valves is exactly mirrorlike only at isolated wavelengths, typically at only a single wavelength in the operating spectral range. We have shown that to avoid contrast loss from the compound-angle depolarization mechanism when the light valve is mirrorlike, the optical system must not induce any rotation in the polarization of skew rays illuminating the light valve. On the other hand, ellipticity induced in the illumination will automatically be canceled out in the return pass through the optics. Pure rotation in the illuminating light can be converted to pure ellipticity by placing a quarter-wave retarder on top of the light valve.

This rule for depolarization of skew rays by projection optics is opposite to what is required of the light-valve active layer itself: In dark state the active layer of a reflective light valve should not introduce ellipticity in the polarization of the central ray (when the ray reaches the mirror backplane); on the other hand, any rotation of polarization that it might introduce will be canceled out in the return pass through the active layer.

At most wavelengths, TNLC light valves in dark state do not behave exactly as mirrors. We have derived in Equation (58) an expression for their contrast loss in an optical system which induces both ellipticity and rotation in the illuminating polarization. Equation (52) generalizes further, presenting the solution for a general polarization-modulating light valve in a general optical system. Equation (52) and the first form of Equation (57) apply to any reflective light valve whose active layer is lossless (or has equal attenuation in the two polarizations). Dark-state intensity of such a light valve in a projector increases with the square of the angular extents of the beam, i.e. for an aligned and telecentric system, as  $NA^2$ .

Finally, the second form in Equation (57) applies whenever the light-valve contrast is large compared to 1 (the case of primary practical importance). Equation (57) shows that one part of the single-pass depolarization introduced by the optics is canceled in the second pass that follows reflection from the light valve, while the remaining portion is doubled (in amplitude, quadrupled in intensity). The portion that is doubled over the round trip is the portion in quadrature with the light-valve depolarization. (This portion is the rotational depolarization when the light valve is mirrorlike.)

The case of a TNLC light valve interacting with a simple PBS optical



system has been explored in some detail, both with and without an added quarter-wave retarder to improve contrast. With no quarter-wave retarder, a rule of thumb is that the dark-state background can be estimated as  $B \approx NA^2/n_{\text{PBS}}^2 \sim NA^2/3$  [see Equations (70) and (71)].

## Acknowledgments

The authors gratefully acknowledge the help of Steve Lovas in fabricating light valves and optical components used in this study. We also thank Hideo Kawakita and Kunio Enami of IBM Japan for many helpful discussions.

## References

*Received April 21, 1997; accepted for publication February 10, 1998*

## Footnotes

<sup>1</sup> For example, Balzers Thin Films Products Division, Fremont, CA; Spectra-Physics Components and Accessories Division, Mountain View, CA.

<sup>2</sup> References pointed out by an anonymous reviewer brought to our attention the work of Ong [15], who analyzed LC light valves in terms of the depolarization (denoted  $\chi$  by Ong), rather than Jones matrices. It might have been easier to integrate our optics model with Ong's light-valve formalism instead of the matrix-based approach of Reference [14].

---

[ [Journals home page](#) | [Subscribe/order](#) | [Current issue](#) | [Recent issues](#) | [Description](#) ]

<a href="#">IBM Home</a>	<a href="#">Shop</a>	<a href="#">Contact IBM</a>	<a href="#">Search</a>	<a href="#">Privacy</a>	<a href="#">Legal</a>
--------------------------	----------------------	-----------------------------	------------------------	-------------------------	-----------------------

©1998 IBM Corporation



*Vol 42 No. 3 - High-Resolution Displays*

[ Table of contents: [HTML](#), [ASCII](#) ]

[ This article: [HTML](#), [ASCII](#) ]

Feature article

0018-8646/98/\$5.00 © 1998 IBM

## Nematic LC modes and LC phase gratings for reflective spatial light modulators

by H. [Yang](#) and M. [Lu](#).

Single-domain nematic liquid crystal (LC) devices based on the polarization-rotation effect, the birefringent effect, or both have been investigated for reflective spatial light modulators (SLMs) which use a polarizing beam splitter to separate the input light beam from its orthogonal output beam. We have evaluated each LC mode in terms of its contrast ratio, optical efficiency, operating voltage, and tolerance to cell-gap nonuniformity. We studied the hybrid- aligned and the  $0^\circ$ -,  $45^\circ$ -, and  $63.6^\circ$ -twisted nematic LC modes, which can be operated either normally white (NW) or normally black (NB). We have also investigated the mixed twisted nematic (MTN) and self-compensated twisted nematic (SCTN) modes in NW and the tilted homeotropic mode in NB. Two-dimensional simulations have also been carried out for both NW and NB modes implemented in active-matrix-driven reflective SLMs to elucidate the effect of fringe fields, which tend to generate disclination lines in high-field on-pixels adjacent to low-field off-pixels. Numerical examples are given to illustrate that, for the NB modes, the disclination lines occurring in the field-on bright state appear dark and reduce the optical efficiency. However, for the NW modes, the disclination lines occurring in the field-on dark states generate a light leakage which degrades the contrast ratio. To improve optical efficiency, we have also studied polarization-independent LC phase gratings using patterned alignment with opposite twist angles for reflective SLMs. The basic equations for the diffracted and nondiffracted intensities have been derived. The device parameters, operating voltage, and optical efficiency are given for various cases with a twist angle equal to or less than  $90^\circ$ .

## Introduction

It is well known that reflective spatial light modulators (SLMs) offer some advantages over transmissive SLMs, such as increased aperture ratio and more compact optical systems [1]. Recently, Alt [1] and Melcher et al. [2] reported a prototype rear projector having a resolution of 2048 by 2048 pixels using three Si-wafer-based liquid crystal (LC) SLMs which utilized a 45°-twisted nematic [or hybrid field-effect (HFE)] mode [3].

Liquid crystals have been widely employed as the display medium for both transmissive and reflective SLMs. In general, the electric-field-tuned LC medium can modulate incident light by one of the following effects: birefringence, polarization rotation, absorption, or scattering. For the active-matrix (AM)-driven transmissive SLMs, the polarization-rotation effect of a 90°-twisted nematic (TN) cell has most frequently been utilized. Operated in the normally white condition, the TN cell for a transmissive display has the advantages of a single cell gap for red, green, and blue colors, low operating voltage, high contrast ratio, high optical efficiency, and insensitivity to variation in cell gap. However, for reflective SLMs with a reflective electrode built inside the LC cell, the TN cell is not useful, because there is no place for a second crossed polarizer. Among reflective nematic LC modes, there is no direct analogy to the transmissive TN mode. Therefore, finding the best LC mode for reflective SLMs is very important.

In this paper, we evaluate single-domain nematic liquid crystal (LC) devices based on the polarization-rotation effect, the birefringence effect, or both for reflective SLMs which use a polarizing beam splitter to separate the input light beam from its orthogonal output beam. We study each LC mode in terms of its contrast ratio, optical efficiency, operating voltage, and tolerance to cell-gap nonuniformity. Our studies include the hybrid-aligned and the 0°-, 45°-, and 63.6°-twisted nematic LC modes, which can all be operated in either the normally white (NW) or normally black (NB) modes. We have also investigated the mixed twisted nematic (MTN) and self-compensated twisted nematic (SCTN) modes for NW and the tilted homeotropic mode for NB. In general, the NW modes have better tolerance to cell-gap nonuniformity than the NB modes, except for the tilted homeotropic mode. We have evaluated the display performance of each LC mode in detail.

Since the pixel for reflective SLMs is usually very small, the effect of fringe fields between high-field on-pixels and low-field off-pixels becomes important. In order to study the fringe-field effect, we have carried out two-dimensional simulations to study LC director<sup>1</sup> orientations and light reflectance as a function of position for reflective active-matrix-driven SLMs. Numerical examples are given for both the NB and NW modes to illustrate the importance of fringe-field effects.

Since the polarization-dependent LC devices use only half of the incident light, it is worthwhile to study the scattering or diffracting LC devices which are polarization-independent and hence offer the potential for a factor-of- 2 increase in optical efficiency. The last part of this paper is devoted to the study of polarization-independent LC phase gratings made by patterned alignment with opposite twist angles for reflective SLMs. We derive the general equations for diffracted and nondiffracted intensities using a Jones-matrix approach. We study the operating voltage and the optical diffraction efficiency for various pattern-aligned LC phase gratings with twist angles equal to or less than  $90^\circ$ . The results for several LC phase gratings have been tabulated and compared.

## Single-domain nematic LC modes

Using nematic LC mixtures with positive dielectric anisotropy<sup>2</sup>, the construction of single-domain nematic LC cells is relatively simple. The nematic LC medium has a thickness,  $d$ , and is sandwiched between two substrates, with the top substrate being transparent and the bottom substrate having a reflective electrode adjacent to the LC medium. There usually exist LC alignment layers such as rubbed polyimide films between the substrates and the LC medium to align the LC director parallel to the rubbing direction with a small pretilt angle ( $\sim 1^\circ$ - $5^\circ$ ) from the substrate plane. The LC director twists through the LC medium from the bottom toward the top substrate with a total twist angle,  $\Phi$ . The Jones matrix [4] of such a reflective nematic LC cell can be written<sup>3</sup> [5] as

$$J(\Phi, \beta) = \begin{pmatrix} (\Phi/\gamma)^2 + (\beta/\gamma)^2 \cos 2\gamma & -i\Phi\beta(1-\cos 2\gamma)/\gamma^2 \\ -i(\beta/\gamma) \sin 2\gamma & -i\Phi\beta(1-\cos 2\gamma)/\gamma^2 + (\Phi/\gamma)^2 + (\beta/\gamma)^2 \cos 2\gamma \\ & +i(\beta/\gamma) \sin 2\gamma \end{pmatrix}, \quad (1)$$

where  $\beta = \pi d \Delta n / \lambda$ ,  $\gamma = \sqrt{\beta^2 + \Phi^2}$ , and  $\Delta n = n_e - n_o$  are the difference between the indices of refraction of the extraordinary and ordinary rays of the LC medium, and  $\lambda$  is the wavelength of the incident light.

Since we are interested in this paper only in LC SLMs which use a polarizing beam splitter to separate the incident beam from the orthogonal output beam, there are three important parameters,  $\Phi$ ,  $\beta$ ,  $\psi$ , where  $\psi$  is the angle between the polarization direction of the incident light and the LC director adjacent to the entrance side of the glass plate. By changing these three parameters, we can completely describe the following LC modes:  $0^\circ$ -,  $45^\circ$ -,  $63.3^\circ$ -twisted, mixed TN, and self-compensated TN. Once we choose an LC mode, the values for  $\Phi$  and  $\psi$  are fixed. The only common variable parameter for all of these modes is  $\beta$ .

Assuming that the polarized incident light is a P-wave, the reflected signal will be an S-wave orthogonal to the P-wave. We can calculate the P-to-S conversion efficiency (PCE) of various LC modes as a function of  $d\Delta n/\lambda$ . By our definition, the PCE characterizes the effect due to the LC medium alone, neglecting loss due to reflection from all surfaces. The results are shown in **Figure 1** for the 0°-, 45°-, and 63.6°-twisted modes and in **Figure 2** for the mixed TN (MTN) and self-compensated TN (SCTN) modes. The values of  $\phi$  and  $\psi$  for different LC modes associated with **Figures 1** and **2** are explained below.

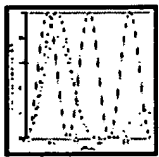


Figure 1



Figure 2

### Homogeneous (or 0°-twisted) LC mode

In this mode,  $\phi = 0^\circ$  and  $\psi = 45^\circ$ ; the LC cell behaves as a birefringent plate with its optical axis at  $45^\circ$  with respect to the crossed polarizer and analyzer. In the literature [6] it is also referred to as parallel-aligned mode. The equation to calculate the PCE can be written as

$$I_{PS} = \sin^2(2\pi d\Delta n/\lambda),$$

and its results as a function of  $d\Delta n/\lambda$  are shown in **Figure 1** as the solid curve. We can operate this mode as NW or as NB. For the NB case,  $I_{PS}$  should be as small as possible when the applied voltage is below the threshold voltage. To satisfy the above condition, there are multiple choices for the cell gap satisfying the equation  $d\Delta n/\lambda = 0.5, 1, 1.5, 2, \dots$  corresponding to half-wave plate, full-wave plate, etc. The voltage required to drive these modes with maximum PCE is quite low (less than 3.5 V) for the case of the half-wave plate and progressively lower for the case of the full-wave plate, etc. One always chooses the half-wave plate to achieve faster response for the SLM. However, it requires stringent cell-gap uniformity to achieve a high contrast ratio. From Equation (2), it can easily be derived that, for contrast ratios larger than 100 to 1,  $|\Delta d/d|$  must be less than 0.032. Equivalently, for a broadband incident light with  $\Delta\lambda/\lambda > 0.032$ , it is impossible to obtain contrast ratios that are larger than 100 to 1. Hence, this mode is only suitable for nearly monochromatic incident light with stringent requirements on cell-gap uniformity.

We can also operate the homogeneous LC mode as NW. Again, there are multiple choices for the cell gap satisfying the condition  $d\Delta n/\lambda = 0.5n + 0.25$ , where  $n$  is an integer. One usually takes  $n = 0$  to satisfy the quarter-wave condition. In this quarter-wave NW mode, the PCE decreases as the applied voltage increases across the LC cell. However, it requires a relatively high voltage (usually larger than 15 V) to achieve a sufficiently dark state for a high contrast ratio because of the residual

birefringent effect caused by the boundary LC layers. The advantage of this mode is the fast response [6], which is sufficient for field sequential color because of its thin cell gap and high operating voltage. The operating voltage can be reduced by placing a properly designed optical compensation film in front of the LC cell. However, the time required to turn on the LC cell increases with a reduced operating voltage.

### 45°-twisted mode

This mode [3] has  $\phi = 45^\circ$  and  $\psi = 0$  or  $90^\circ$  and has been referred to as the HFE (hybrid field-effect) mode. The equation for the PCE in the case of zero field can be written as

$$I_{PS} = [1 - \pi^2 / (16\gamma^2)] \times \pi^2 \sin^4 \gamma / (4\gamma^2), \quad (3)$$

and the results as a function of  $d\Delta n/\lambda$  are shown as the dotted curve in Figure 1. For the NB operation, we usually choose  $d\Delta n/\lambda = \sqrt{15/16}$  so that  $\sin \gamma = 0$  in Equation (3).

In order to find the PCE as a function of applied voltage, we have to carry out further simulations. For the calculation of the LC director profile across the LC cell under an applied electric field, we have used a tensor formulation [7] of LC continuum theory, allowing full elastic anisotropy, chirality, and disclination [8]. Such a method was also applied for the 2D simulation described in a later section of this paper. The extended Jones-matrix method [9] was used to calculate the PCE of LC cells with monochromatic incident light.

The operation voltage for this mode [3] is usually less than 3.5 V. We have verified this low operating voltage by calculating the PCE as a function of applied voltage. The results are shown in **Figure 3**. For the calculation of Figure 3, we used the data for LC mixture MLC13200-100 from Merck & Co., Inc., and other parameters listed in **Table 1**. The cell-gap tolerance for this mode can be derived from Equation (3) and is large, so that, for  $|\Delta d/d| \leq 0.11$ , the contrast ratio exceeds 200 to 1. The disadvantage of this mode is a low PCE (less than 0.93), as shown in Figure 3. The PCE can be improved to better than 0.99 by changing the twist angle from  $45^\circ$  to about  $54^\circ$  [10]. However, at a twist angle of  $54^\circ$ , the tolerance to cell-gap nonuniformity is slightly less [10] than with the  $45^\circ$ -twisted mode.

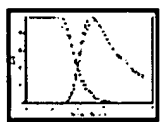


**Figure 3**

**Table 1** Parameters used for the calculation of Figure 3 with incident wavelength at 546 nm.

<i>Device</i>	<i>Mode</i>	$\Delta n d / \lambda$
MTN	NW	0.45
SCTN	NW	0.62
45°-twist	NB	0.97
54°-twist	NB	0.95

We can also operate the 45°-twisted mode as NW by choosing  $d\Delta n/\lambda = 0.362$ . The advantage is a relatively fast response time because of a thin cell gap as compared to the NB mode, but it requires relatively high voltage to achieve high contrast ratio and has a low PCE (about 0.81).

- *63.6°-twisted mode*

This mode [11] has  $\phi = \pi \div 2\sqrt{2}$  and  $\psi = 0^\circ$  or  $90^\circ$ . The equation for the PCE can be simplified as

$$I_{PS} = \phi^2 \beta^2 (1 - \cos 2\gamma)^2 / (\gamma^4), \quad (4)$$

and the results as a function of  $d\Delta n/\lambda$  are shown in Figure 1 as the dashed curve. We can choose  $d\Delta n/\lambda = 0.935$  or  $0.354$  for NB or NW operation, respectively. The characteristics of 63.6°-twisted NB and NW modes are similar to the corresponding 45°-twisted NB and NW modes, except that the 63.6° NW mode has a nearly 100% PCE, as indicated in Figure 1.

#### *Hybrid-aligned cell*

The hybrid-aligned mode [12] is similar to the 0°-twisted mode, except that the LC directors adjacent to one of the cell substrates are aligned perpendicular or nearly perpendicular to the cell substrate. The equation for the PCE can be expressed as in Equation (2) with  $\Delta n$  replaced by  $0.5 \Delta n$  because the effective birefringence of the hybrid-aligned LC cell is a factor of 2 less than the 0°-twisted cell. For the NW hybrid-aligned mode, there is no threshold voltage, and it requires a relatively high operating voltage to achieve good dark states because of the existence of residual birefringence due to the boundary LC layers. It has the advantage of fast response time because of a relatively thin cell gap and hybrid alignment, so that an external field exerts a high torque instantaneously on the LC directors in the cell. For the NB operation, it requires very stringent cell-gap uniformity, as in the case of the NB 0°-twisted mode.

#### *Mixed TN mode*

The mixed [13] TN mode has  $\phi = 90^\circ$  and  $\psi = 20^\circ$ . The PCE of the MTN mode as a function of  $d\Delta n/\lambda$  is shown as the solid curve in Figure 2. For the NW operation, the cell gap is chosen to satisfy the equation  $d\Delta n/\lambda =$

0.45. We have calculated the PCE as a function of applied voltage, and the results shown in [Figure 3](#) indicate that a voltage larger than 4.5 V is needed for NW MTN. The peak PCE is only 0.88, as shown in [Figure 3](#). However, its turn-on and turn-off times are about four times faster than those of the corresponding 90°-twisted TN cell because of the shorter cell gap. The PCE can be increased by reducing  $\phi$  and changing  $\psi$ . However, when this is done, the operating voltage increases. The NW MTN mode has a large tolerance for cell-gap nonuniformity. As far as  $|\Delta d/d| < 0.15$ , high contrast ratio can be maintained if the dark state is taken at a voltage larger than 4.5 V for most of the useful LC mixtures for AM LCDs. The NB MTN mode is not attractive because it has poor tolerance to cell-gap nonuniformity.

- *Self-compensated TN mode*

The self-compensated [14] TN mode has  $\phi = 60$  to  $65^\circ$  and  $\psi = 0.5\phi$ . The PCE as a function of  $d\Delta n/\lambda$  is shown in [Figure 2](#) as the dashed curve for the case  $\phi = 60^\circ$ . For the NW operation, we chose the cell gap to satisfy the relation  $d\Delta n/\lambda = 0.61$ . The PCE can be 100%, and its operating voltage is the lowest among all of the NW modes discussed in this paper. One of the solid curves in [Figure 3](#) shows the calculated results of PCE as a function of applied voltage for the SCTN with a twist angle of  $60^\circ$ , indicating a high PCE and low operating voltage. The low operating voltage is the result of a partial self-compensation [14] effect between two boundary LC layers adjacent to cell boundaries under the external field because the polarization of the incident beam bisects these two boundary LC layers. The NW SCTN mode has a medium tolerance in cell-gap nonuniformity such that  $|\Delta d/d|$  should be below about 0.1, and an operating voltage below about 3 V is possible by using an LC mixture with larger dielectric anisotropy, such as TL222 from Merck. The SCTN mode is unsuitable for the NB operation because it requires a stringent cell-gap uniformity.

- *Tilted homeotropic mode*

The tilted homeotropic (TH) mode [15], which is also referred to as the DAP (deformation of aligned phase) or ECB (electric-field-controlled birefringence) mode, is suitable only for the NB operation. For the TH mode, we use nematic LC mixtures with negative dielectric anisotropy, and the LC directors are aligned approximately perpendicular to the substrates of the LC cell, with a small pretilt angle away from the normal of the cell substrate. The TH cell is placed between crossed polarizers whose polarization directions are bisected by the projection of the LC directors onto the cell substrate. When the applied voltage across the TH cell is larger than the threshold voltage, the LC directors within the TH cell are deformed toward the substrate plane, resulting in an equivalent birefringence plate. The PCE of a TH cell under applied external voltage can reach 100% and can be described by the integration of Equation (2) across the cell thickness, where  $\Delta n$  is no longer a constant but depends on the position across the TH cell. The quiescent state is the dark state of



the display. The dark state becomes less dark as the pretilt angle from cell normal increases. For high contrast ratio, the pretilt angle from cell normal should be less than  $\sim 4^\circ$  if we choose  $d\Delta n/\lambda < 0.5$ . The major advantages of the TH cell are extremely high contrast ratio, high PCE, a single LC thickness for red, green, and blue colors, and a very large tolerance to LC thickness nonuniformity (the tolerance is  $|\Delta d/d| \geq 0.15$ ). The disadvantages are difficulty in achieving stable alignment and limited availability of LC mixtures with negative dielectric anisotropy.

### Fringe-field effects

The pixel for reflective SLMs is rather small, about 5 to 20  $\mu\text{m}$ . In order to achieve a high aperture ratio, the gap between each pixel electrode is very small, of the order of 1  $\mu\text{m}$ , depending on the photolithographic rules. If a pixel is switched on with the adjacent pixels off, the fringe field between the on-pixel and adjacent off-pixels will generate two effects. Parts of the off-pixel adjacent to the on-pixel will be partially switched on, and parts of the on-pixel will be on to a smaller extent. This will result in a change of the modulation transfer function of the display. The second effect is that disclination lines will be generated within the on-pixel as a result of competition between the normal-tilt domain under uniform field and the reverse-tilt domain generated by the fringe field. In the NB case, the disclination lines appear dark within the bright on-pixel to reduce the effective aperture ratio. However, in the NW case, the disclination lines appear bright within the dark voltage-on pixel, thereby reducing its contrast ratio.

We have carried out a two-dimensional simulation to study the effects of the fringe field on the display. **Figure 4** shows the construction of a  $45^\circ$ -twisted LC mode in a reflective SLM. On top of a silicon substrate, we deposited a 200-nm metallic light-absorbing black matrix with  $n = 0.89$  and  $k = 1.51$ , where  $n$  and  $k$  are the real and imaginary parts of the index of refraction, respectively. A silicon nitride layer of 450 nm was deposited between the black matrix and the Al pixel electrode with a thickness of 150 nm. The pixel is 15  $\mu\text{m}$ , with a gap of 2  $\mu\text{m}$  between the pixel electrodes. The LC cell gap is 2.65  $\mu\text{m}$  and, for the simulation, we used data for the LC mixture TL222 from Merck with a chiral pitch of 32  $\mu\text{m}$ . The indium- tin-oxide (ITO) electrode has a thickness of 140 nm. As shown in **Figure 4**, the LC directors twist from a position  $45^\circ$  between the  $x$ - and  $-y$ -axes on the pixel electrode to the  $-y$ -axis on the ITO electrode. The LC directors have a pretilt angle  $\alpha$  of  $2^\circ$  from the substrate plane.

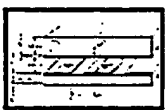
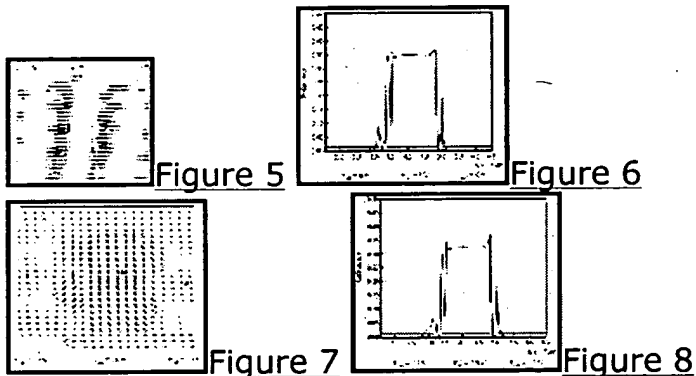


**Figure 4**

To illustrate the fringe-field effect on an NB display, the LC director orientations and reflectance have been calculated along a middle line in the  $x$ -axis direction across a three-pixel geometry. Both the ITO electrode

and the black matrix are connected to ground potential. In the first case, pixels 1 and 3 are at ground potential, while pixel 2 in the middle is at 3 V. The results for the LC director orientation are shown in **Figure 5**, where the grid points for calculation are finer in the gap region between pixel electrodes. The results indicate that a disclination line located to the left of the center of the on-pixel exists at 3 V. The disclination separates the normal-tilt domain at the right from the reverse-tilt domain at the left. The reverse-tilt domain is caused mainly by the fringe field existing on the left edge of the pixel electrode at 3 V. The calculated reflectance associated with **Figure 5** is shown in **Figure 6**, which indicates the existence of a dark disclination line on the bright on-pixel and the fringe field turning a small portion of the adjacent off-pixel partially on. For comparison, we have also calculated the case in which pixels 1 and 3 are at 1.5 V instead of 0 V. The results for the LC director orientation and the reflectance are shown in **Figures 7** and **8**, respectively. Comparing **Figures 5** and **7** or **Figures 3** and **8**, the fringe-field effect is rather insensitive to the off-pixel from 0 to 1.5 V.



To illustrate the effect of fringe field on an NW display, we have also carried out two-dimensional simulation for NW SCTN with a total twist angle of  $60^\circ$  such that the LC directors twist left-handed from the pixel electrode toward the ITO electrode, with the  $-y$ -axis bisecting the total twist angle. (See **Figure 4** for reference.) The data of the LC mixture ZLI3449-100 from Merck were used for simulations. The pixel is  $17\text{ }\mu\text{m}$ , with a gap of  $1.8\text{ }\mu\text{m}$  between pixel electrodes. The LC cell gap is  $2.6\text{ }\mu\text{m}$ . Simulations were made with three pixels using voltages of -2.5, 2.5, and -2.5 V in sequence, with both the ITO electrode and the metallic black matrix grounded. The simulated results for LC director orientations as a function of position along the  $x$ -axis are shown in **Figure 9**, and the corresponding reflectance is shown in **Figure 10**. Again, in **Figure 9**, the grid points are finer around the gap region to elucidate the fringe-field effect. **Figure 9** indicates that there exists a reverse-tilt domain around the left edge of the central pixel electrode. There exist two disclination lines, one to the left and the other to the right of this reverse-tilt domain. A strong light leakage occurs around each disclination line, as shown in **Figure 10**. In this case, the light leakage is quite large, so that extreme care must be taken in designing and driving various LC modes for NW operation.

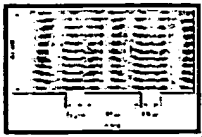


Figure 9

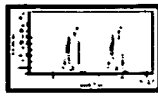


Figure 10

## Conclusions concerning single-domain nematic LC modes

We have investigated several different LC modes for reflective SLM applications. The selection of the best LC mode depends on specific applications. In general, NW modes may have a high contrast ratio in test cells, but by implementing them on the Si-wafer-based active matrix, a high contrast ratio can be maintained only with a nonreflecting black matrix absorbing the light impinging upon the gaps between pixel electrodes. NB modes are more suitable in the case of a poor black matrix.

For the case of using three SLMs, each for one color, to form a projection display, both NB 54°-twisted and NW SCTN are particularly attractive because of their low driving voltage and high PCE. We have optimized the twist angle of the NB HFE mode to achieve an NB 54°-twisted cell which has nearly 100% PCE, a 7% improvement over the NB HFE (45°-twisted) cell, with a slight reduction in cell-gap tolerance.

Comparing the 54°-twisted NB mode with the TH NB mode, we find that the latter has a slightly larger cell-gap tolerance and higher contrast ratio due to homeotropic alignment, with a relatively low pretilt angle from cell normal. The TH mode is attractive when a high driving voltage (>5 V) is available, and stable uniform alignment with a suitable pretilt angle can be achieved.

For field-sequential color displays using a single cell for full colors, NW modes are generally more favorable than NB modes because of their shorter cell gap, resulting in faster switching speeds. For this application, NW 0°-twisted or 63.6°-twisted mode with an optical compensation film to lower the driving voltage and maintain a high PCE as well as an NW MTN mode with a lower PCE can be used.

## Polarization-independent LC phase gratings

It is well known that polarization-dependent reflective or transmissive LC SLMs use only at most half of the incident light intensity without the use of unwanted polarization, which increases étendue and cost. Scattering and diffracting LC devices have the potential to utilize all of the intensity of the incident light. LC phase gratings are a polarization-independent alternative to the polarization-dependent LC modes discussed in the first part of this paper. Hori [16] proposed an LC grating design based on field-induced tunable birefringence. However, the untwisted device exhibited polarization-dependent performance and required a high voltage to achieve high contrast. It also required interdigitated electrodes

within each pixel, resulting in a possibility of more shorts across electrodes. Fritsch et al. [17] have investigated polarization-independent LC gratings. The result was a reflective device based on the field-controlled birefringence difference between alternating stripes inside each pixel. To avoid using interdigitated electrodes, Shannon et al. [18] suggested the use of pattern alignment to generate phase gratings. Because the differently patterned domains require no separation, diffraction efficiency is increased and the risk of shorts between electrodes is reduced. Bos et al. [19] have demonstrated the use of pattern alignment with an optically active device for transmissive SLMs. High contrast and relatively low-operation voltage have been demonstrated. It is a purpose of this paper to explore the pattern alignment with a periodic unit domain consisting of two equal-size half-domains with opposite twist angle.

In utilizing the polarization-independent LC phase gratings, except for some rare special cases, it is extremely difficult to make the nondiffracted light vanishingly small, so that collecting the nondiffracted light as a signal results in poor contrast. Therefore, in this paper, we consider only the case of collecting the diffracted light as a signal.

Following Equation (1), we can write the output  $E$ -field  $[E_{xo}, E_{yo}]$  after an interference between two domains with opposite twist angles in terms of the input  $E$ -field  $[E_{xi}, E_{yi}]$  as

$$\begin{bmatrix} E_{xo} \\ E_{yo} \end{bmatrix} = ([J(\Phi, \beta)] + [J(-\Phi, \beta)]) \begin{bmatrix} E_{xi} \\ E_{yi} \end{bmatrix}. \quad (5)$$

The resulting intensity, which represents nondiffraction intensity, can be written as

$$I_o = |E_{xo}|^2 + |E_{yo}|^2 = [(\Phi/\gamma)^2 + (\beta/\gamma)^2 \cos 2\gamma]^2 + (\beta/\gamma)^2 (\sin 2\gamma)^2. \quad (6)$$

The diffracted intensity due to interference between two domains can be expressed as

$$I_d = [\Phi\beta/(\gamma)^2(1 - \cos 2\gamma)]^2. \quad (7)$$

From Equation (6), we see that in order to have the nondiffracted (or zero-order-diffraction) intensity  $I_o$  equal to zero, the following two conditions must be satisfied:

$$(\Phi/\gamma)^2 + (\beta/\gamma)^2 \cos 2\gamma = 0 \quad (8)$$

$$\beta(\sin 2\gamma)/\gamma = 0. \quad (9)$$

The solutions for Equations (8) and (9) are

$$\gamma = \left( \frac{2n+1}{2} \right) \pi \text{ and } \phi = \frac{\gamma}{\sqrt{2}}, \text{ where } n = 0, 1, 2, \dots \quad (10)$$

Substituting (10) into (7), we have  $I_d = 1$ , so that all of the incident light becomes diffracted. In this case, we have 100% optical efficiency. The Jones matrix becomes

$$J \begin{pmatrix} \pm (2n+1) \frac{\pi}{2\sqrt{2}}, (2n+1) \frac{\pi}{2\sqrt{2}} \\ 1 \end{pmatrix}_i = \pm \begin{pmatrix} 0 & 1 \\ -1 & 0 \end{pmatrix}. \quad (11)$$

This means that, in the case of 100% optical efficiency, the polarization of incident light has been rotated exactly  $90^\circ$  or  $-90^\circ$  by the SLM. According to Equation (10), there are multiple cases having 100% optical efficiency. But, except for the  $n = 0$  case, these cases have a twist angle larger than  $180^\circ$  and a large  $d\Delta n$ , so that the device will have very long response times. One obvious solution for Equation (10) is that when  $n = 0$ ,  $\phi = \beta = \pi/(2\sqrt{2})$ . The device is diffractive when  $E = 0$ , and diffraction decreases as the field increases. We call this a normally white diffractive (NWD) mode. This NWD mode has 100% optical efficiency, a low twist angle, and a thin cell gap resulting in short response times. The disadvantage of this NWD mode is the high driving voltage required because of the residual birefringence effect caused by the boundary LC layers. The diffraction efficiencies of other opposite-twisted two-domain TN LC phase gratings with a twist angle equal to or less than  $90^\circ$  are less than 100%. For the NWD mode, the device parameters, driving voltage, and optical efficiency for different twist angles are listed in **Table 2**. Although the  $90^\circ$  TN phase grating has a low driving voltage, the optical diffraction efficiency is quite low.

**Table 2 Summary of parameters for LC phase gratings.**

---

$\phi$	$\beta = \Delta n d /$	Mode	$I_D$ (max.)	Voltage [9]
--------	------------------------	------	-----------------	----------------

	$\lambda$		(%)	(V)
0.5 $\pi$	0.355	NWD	69.4	3.3
0.5 $\pi$	0.866	NBD	33.0	2.2
0.3536 $\pi$	0.354	NWD	90.2	>5
0.3536 $\pi$	0.935	NBD	91.8	2.4
0.3 $\pi$	0.36	NWD	100	>5
0.3 $\pi$	0.954	NBD	93.9	2.4
0.25 $\pi$	0.365	NWD	81.4	>5
0.25 $\pi$	0.968	NBD	93.5	2.5

In addition to the NWD modes, we can make the device nondiffractive at zero field, becoming diffractive when the field is on. We call these normally black diffractive (NBD) modes. The requirement for the NBD mode is that the off-diagonal terms of the Jones matrix as expressed by Equation (1) be equal to zero in the quiescent state. That is,

$$\Phi\beta/(\gamma)^2(1 - \cos 2\gamma) = 0, \quad \text{i.e., } \gamma = n\pi. \quad (12)$$

In this case, the Jones matrix becomes a unit matrix at the quiescent state. In Equation (12), once the value of  $n$  is chosen, the value of  $\beta$  can be determined for a given  $\Phi$ . In the on-states, the electric field drives the two reverse-twisted domains into the polarization-rotation state. The driving voltage of the NBD is much lower than the NWD. The optical diffraction efficiencies of the NBD LC phase gratings (calculated for the case of TL222 from Merck) as a function of applied voltage are shown in **Figure 11** for the twist angles of 45°, 54°, 63.6°, and 90°. A diffraction efficiency of nearly 100% can be achieved by using a 54°-twisted instead of 63.6°-twisted LC phase grating because of the nonuniform twist of the liquid crystal molecules in field-on states. For the NBD mode, the device parameters and the estimated optical efficiencies are listed in Table 2.

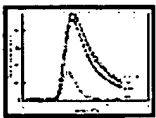


Figure 11

In conclusion, the NWD LC phase gratings have, in general, high operating voltages, but faster response times than the NBD LC phase gratings. Some of the NBD LC phase gratings have low operating voltages as well as relatively high optical diffraction efficiencies, including three having twist angles from 45° to 63.6°. The 54°-twisted NBD mode is extremely attractive because of its nearly 100% optical diffraction efficiency and low operating voltage.

## Acknowledgment

• The authors acknowledge Kun-Wei Lin at Sunplus Technology Co., Ltd., Taiwan, for writing the programs to perform two-dimensional simulations.

## **References**

*Received May 10, 1997; accepted for publication March 1, 1998*

## **Footnotes**

<sup>1</sup>The term *director* refers to the direction of the long molecular axis of liquid crystal.

<sup>2</sup>In positive dielectric anisotropy, the difference between dielectric constants along and perpendicular to the LC director is positive.

<sup>3</sup>Our results are different in sign from the results of Lu and Saleh [5].

---

[ [Journals home page](#) | [Subscribe/order](#) | [Current issue](#) | [Recent issues](#) | [Description](#) ]

<a href="#">IBM Home</a>	<a href="#">Shop</a>	<a href="#">Contact IBM</a>	<a href="#">Search</a>	<a href="#">Privacy</a>	<a href="#">Legal</a>
--------------------------	----------------------	-----------------------------	------------------------	-------------------------	-----------------------

©1998 IBM Corporation



*Vol 42, No. 3 - High-Resolution Displays*

[ Table of contents: [HTML](#), [ASCII](#) ]

[ This article: [HTML](#), [ASCII](#) ]

Feature article

0018-8646/98/\$5.00 © 1998 IBM

## **A one-megapixel reflective spatial light modulator system for holographic storage**

by J. L. Sanford, P. F. Greier, K. H. Yang, M. Lu, R. S. Olyha, Jr., C. Narayan, J. A. Hoffnagle, P. Alt and R. Melcher.

**A prototype reflective spatial light modulator (SLM) system has been developed for writing megabit pages of data into a holographic medium at a rate of 12 pages per minute. The SLM is based upon a crystalline-silicon reflective active-matrix array with integrated data drivers, using liquid crystal (LC) electro-optics and a personal computer system with an interface to provide data. The LC has been optimized for high contrast and efficiency with coherent illumination. The resolution-limited contrast was measured at 4:1, which was high enough to provide bit-error-free charge-coupled-device images using modulation and error-correction codes.**

### **Introduction**

Recent development in spatial light modulators (SLMs) is helping to make volume holographic storage for digital data a reality [1, 2]. SLMs consist of one- or two-dimensional arrays of light-modulating elements. Silicon technology as used in projection data monitors is now capable of producing small-sized, two-dimensional light-valve arrays having several hundred thousand to several million light-modulating elements. This allows imaging or writing very large amounts of information at one time. Given high image-update rates, high data-writing rates are possible. With increases in the speed of writing and reading with high-speed charge-coupled-device (CCD) cameras, holographic recording may be able to compete with other recording technologies. Efficient compact recording systems are possible through the use of projection-display reflective-silicon light-valve technology [3]. The reflective-silicon light-valve technology has a high aperture ratio and the ability to match its pixel size with the CCD camera pixel size.

The development focus of our prototype holographic-recording reflective SLM system was aimed at 1) suitable light modulation of the LC; 2) the silicon back-plane or chip design; 3) a system to provide data to the SLM at a sufficient writing rate; and 4) testing of the SLM as it relates to holographic recording.

### **Reflective SLM holographic recording**

<http://www.research.ibm.com/journal/rd/423/greier.html>

11/7/2000



In developing an SLM system suitable for holographic recording, it is useful to look at how a reflective SLM is used in a holographic recording. Holographic recording is accomplished by the interference of an image beam and a reference laser beam within a holographic recording medium--in this case, a photorefractive material such as  $\text{LiNbO}_3$ .

The optical interference pattern causes charges to be excited from impurity centers. After diffusion and re-trapping, the redistributed charge forms a grating in the photorefractive medium. Depending upon the medium material, a fixing process for long-term storage of data may be required. When the medium is exposed to only the reference beam, the light will diffract to reproduce the image. **Figure 1** shows the basic elements of a holographic data storage system. The spatial light modulator converts the digital data of ones and zeros into a two-dimensional array of bright and dark spots. The Fourier plane image of the array is the image to be stored in the holographic medium. A uniform laser beam is directed in an orthogonal manner onto the reflective surface of the SLM by a polarizing beam splitter (PBS). The PBS allows the polarization-converted image to be focused into the holographic medium. The reconstructed data are imaged onto a CCD camera system, which detects the reconstructed hologram as digital information. Multiple images comprising a stack can be written separately into the same volume of the holographic medium by changing the angle of the reference beam or by selection of multiple reference beams into the medium. Multiple stacks provide the desired system capacity.

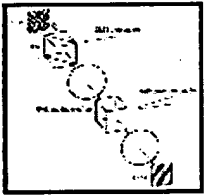


Figure 1

The method of producing the image beam for writing consists of sending data to the SLM while it is addressed by rows from top to bottom. The pixels retain their voltage long enough for the array to be addressed and exposed. The LC must respond to the voltage excitation of the last row in the array before the SLM image is illuminated. To avoid dc voltage across the LC, which may cause image sticking, the polarity of the pixel voltage is reversed in the next frame. The amount of exposure time depends upon the holographic material and on available laser power. The minimum exposure for  $\text{LiNbO}_3$  is between 50 and 100 milliseconds.

## Reflective twisted nematic liquid crystal

Development was focused on the properties of LC light modulation as it pertains to holographic recording. We concentrated on twisted nematic (TN) normally black (NB) LC modes, since they offer higher contrast with low drive voltages as compared to normally white (NW) modes [4]. The PBS allows efficient illumination and cross-polarization for NB operation with reflective SLMs. The normally black LC crystal mode provides electro-optic modulation by changing the polarization of reflected light by  $90^\circ$  with about  $3 V_{\text{RMS}}$  applied, while leaving the polarization unchanged for zero (or low) applied voltage.

The cover glass has a transparent indium-tin oxide (ITO) conductor on the inside surface. On the cover-glass ITO and on the SLM mirror surfaces, thin polyimide layers are deposited and rubbed to provide for LC alignment. The LC molecules align with the rubbing direction. The ITO voltage is held constant at 3 V, and a 0-6-V square-wave voltage is applied to the pixel mirrors for LC electro-optic modulation. The equivalent of a transmissive  $90^\circ$ -twisted nematic LC mode is the reflective  $45^\circ$ -twisted nematic LC mode. **Figure 2** depicts the reflective  $45^\circ$ -twisted nematic LC operation. The rubbing direction on the mirrors is rotated  $45^\circ$  relative to the rubbing direction on the cover glass, providing a  $45^\circ$  twist in LC alignment between the two surfaces. The incoming polarized illumination is aligned with the rubbing direction of the cover glass. As the incoming illumination passes through the LC, the polarization is rotated  $45^\circ$ . After

reflection, the direction of polarization and its rotation are reversed. Upon exiting the SLM, the polarization is the same as the incoming polarization. With applied voltage, the LC molecules try to orient with the electric field, which is perpendicular to the cover-glass and SLM surfaces. The incident light theoretically becomes nearly circularly polarized as it reaches the mirror. After reflection, polarization becomes nearly linear again as it exits the cell, but is rotated  $90^\circ$ . If perfectly linear, the polarization conversion would be 100% efficient. Efficient polarization conversion for wavelengths and LC materials of interest was obtained by detailed LC modeling, cell fabrication, and evaluation.

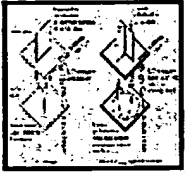


Figure 2

- *LC modeling*

Modeling of the electro-optical properties of LC spatial light modulators in order to optimize the modulator qualities in terms of contrast ratio, polarization conversion, and cell-gap fabrication tolerances has become increasingly important, because all relevant parameters may be varied easily and certain relations may be investigated specifically. The computer simulation of the static electro-optical behavior has been done in two steps. First, the orientation of the nematic director as a function of distance from each cell surface has to be computed. The theoretical analysis of the LC director profile in a cell with an applied field has been well documented in the literature [5-7]. We followed the papers by Deuling [6, 7] for the computations of the nematic director profile in the LC cell as a function of applied voltage.

The second step of the simulation deals with light propagation in the quiescent and deformed LC media, which are inhomogeneous and uniaxial. Although many methods have been developed for this application, we have made our computations based on the Jones-matrix method [8] and the  $4 \times 4$  matrix method described by Berreman [9] and by Wohler et al. [10]. We have found that at near normal incidence, the computed polarization-conversion efficiency of the Jones-matrix method, which ignores the reflection due to the interface between any two dielectric media, has a negligible difference from the result of the  $4 \times 4$  matrix method, provided that the reflective SLM has less than 0.5% reflection between the air and the cover-glass window. This is achieved by using antireflection coatings on the glass window and by making the ITO thickness approximately equal to half of the incident wavelength. We have constructed our SLMs to satisfy the latter two conditions. Hence, we have used the Jones-matrix method for both quiescent and deformed SLM states to take advantage of the polarization-conversion efficiency of the quiescent state of the SLM offered by the Jones-matrix method [4]. This facilitates our analysis of the quiescent state as the dark state of the SLM, to estimate the contrast ratio as well as the cell-gap tolerance.

#### *Quiescent (uniformly twisted) states*

The LC polarization-conversion efficiency is determined by the bright or "on" state behavior, while the LC contrast ratio is mostly determined by the dark or "off" state. The dark state of the reflective twisted nematic LC normally black mode is determined by the twist angle and the quantity  $d\Delta n/\lambda$ , where  $d$  is the cell gap,  $\Delta n$  is the anisotropy of the index of refraction of the LC material, and  $\lambda$  is the wavelength of the illuminating light. The Jones matrix is used to find an initial design point for different LC twist angles, assuming uniform twisting of LC molecules between the SLM mirror and the cover-glass surfaces. We also assumed that the LC molecules have a small uniform tilt angle (about  $2^\circ$ ) from the substrate surface across the LC cell. **Figure 3** shows calculated polarization-conversion efficiencies as a function  $d\Delta n/\lambda$  for the  $45^\circ$ - and  $63.6^\circ$ -twisted angles. The polarization-conversion efficiencies are approximately 82% and 100%,

respectively. For operation in the normally black mode, liquid crystal cells should be fabricated at the first minimum, where  $d\Delta n/\lambda = \sqrt{1 - (\alpha/\pi)^2}$  and  $\alpha$  is the twist angle; i.e., for  $\alpha = \pi/4$ ,  $d\Delta n/\lambda \approx 1$ . Test cells built and measured in the deformed states or "field-on" states showed that the 45°-twisted cells had higher polarization-conversion efficiency than 63.6°-twisted cells. This indicated to us that we cannot optimize the LC performance on the basis of the quiescent state alone.

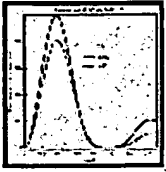


Figure 3

#### *Deformed and tilted state (nonuniformly twisted)*

The deformed state is characterized by nonuniform tilting and twisting of the LC director. The director tries to align with the applied electric field but is constrained at the surfaces, so the orientation in the middle of the cell is a balance between the electric driving force and the elastic restraining forces. The resulting configuration is different from the quiescent configuration, as is the polarization-conversion behavior. The polarization-conversion efficiencies based upon deformed states as a function of the twist angle of the quiescent LC cell are shown in **Figure 4**. The conversion efficiency as a function of voltage is shown in **Figure 5**. Both figures show a polarization-conversion efficiency of approximately 93% and 100% for the 45°- and 54°-twisted angles, respectively. Both twist angles have contrast better than 200:1 with  $\pm 7\%$  dark-state assembly tolerance. Assembled SLMs have also shown that the 54°-twisted nematic LC has excellent efficiency, as well as large-area contrast with good assembly tolerance.

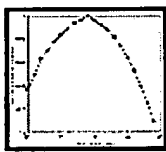


Figure 4

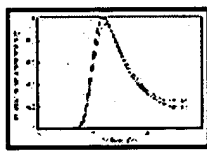


Figure 5

#### *Resolution-limited contrast*

Large-area contrast is an important measure of cell uniformity and process control and is very important in display applications. For holographic storage, resolution-limited contrast rather than large-area contrast is a more useful design criterion, since the data being stored may not be images and may lack spatial correlation. The use of modulation, interleaving, and error-correction codes further reduces the spatial coherence of the SLM image.

Typically, even SLMs having high large-area (all-on to all-off) contrast ( $>100:1$ ) will have much lower (about 4:1) pixel-resolution-limited (adjacent-pixel-on-to-off) contrast. The difference is due to a variety of effects, including scattered light from irregularities in the cell at the subpixel level; three-dimensional effects due to size and placement of spacer posts and to LC disclinations arising from the resulting fringing electric field at the pixel edges; electrical crosstalk between adjacent pixels; and index mismatching of the layers within the LC cell with the use of coherent illumination. Scattering, index mismatching, and three-dimensional effects appear to dominate the resolution-limited contrast in twisted nematic liquid crystal SLMs.

- Scattered light from irregularities in the cell can be reduced with improvements in via design, mirror design, metallurgy, and fabrication [11].
- The decision to use the normally black mode was fundamental to reducing the impact of three-dimensional effects (disclinations) on the large-area contrast ratio. The disclinations affect the on-pixel brightness but not the off-pixel dark level. In addition, we have observed that the impact of disclinations on resolution-limited

contrast is a function of the field difference between adjacent on and off pixels. Improvement in resolution-limited contrast has been obtained by driving all of the pixels in one frame with the same polarity and optimizing the off-pixel voltage to reduce the on-to-off-pixel voltage difference. Unlike displays, holographic storage is not sensitive to flicker, eliminating the need for row-, column-, or pixel-voltage polarity inversion. As a result, the zero electric field between pixels having the same optical state provided by frame inversion is used to eliminate the disclinations. As shown in **Figure 6**, if the off-pixel voltage is increased from 0  $V_{RMS}$  to 1.5  $V_{RMS}$ , the disclinations are reduced in size and move into the space between the mirrors. The disclinations are virtually eliminated while providing an improvement in the resolution-limited contrast.

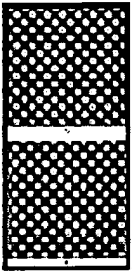


Figure 6

To further understand and quantify the sources of scattered light, confocal microscopy [12] has been used. The confocal microscope provides very high-resolution images using a scanning laser and a linear CCD array. The very low numerical aperture of the system does not allow most of the scattered light to be detected. To first order, the point-by-point variation in intensity of the sum of images with and without a quarter-wave plate is due to absorption and scattering. Lasertech Model 1LM21 H confocal microscope images of a 45° TN SLM with and without a quarter-wave plate at best focus are shown in **Figure 7**. A repeated pattern having one pixel driven on at 3.1  $V_{RMS}$  with surrounding pixels driven at 0  $V_{RMS}$  is shown. The disclinations through the pixel and field-effect-illuminated regions around the pixel can be seen in the image without the quarter-wave plate. The via connecting the mirror and hillocks in the aluminum mirror surface are clearly shown in the quarter-wave-plate image. A bitmap-image-manipulation software program was used to produce the scattered and absorbed light image in **Figure 8**. On an image point-by-point basis, the two images in **Figure 7** were added and the difference from maximum intensity obtained. The outline of the mirrors, disclinations, mirror via, mirror hillocks, and leading-edge rubbing-direction effects at the left and bottom edges of the on-pixels are seen as bright areas. The circular object visible in the lower left corner of the image is a spacer post used to control the cell gap. The edges of the spacer post also contribute to scattered light.

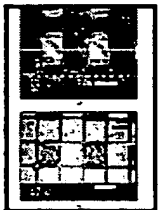


Figure 7

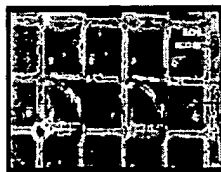


Figure 8

Pixel-to-pixel electrical crosstalk is not observed in our SLMs, apparently owing to the use of a fixed-potential-connected conductive light-absorbing layer just under the mirrors and a ground-connected substrate.

Initial characterization of 45°-twisted SLMs using coherent illumination revealed nonuniformity as high as 25%. Adding a broadband antireflection coating to the top glass virtually eliminated the interference of long-coherence-length light that reflected off the SLM cover glass and the bottom surface of the polarizing beam splitter. However,

5% ringlike nonuniformity remained. A second source of interference was found to be a result of cell-gap variation. A spectral scan was performed on an unexcited 45°-twisted SLM using an analyzer parallel to the polarized incident illumination. It showed 10-20% intensity ripples with a peak-to-peak spacing of 7% of the wavelength. These are Fabry-Perot peaks arising within the SLM due to optical index mismatch at the LC/ITO interface. The ripple intensity was a minimum at about 550 nm, which corresponds to the half-wave design thickness of the ITO. Similarly, if the cell gap varies with a single wavelength, this is equivalent to a wavelength shift and can produce similar levels of nonuniformity. We performed an interference analysis as a function of wavelength and cell-gap variation. The optical path-difference analysis with wavelength gave  $\Delta\lambda = \lambda^2 / (2nd) = 0.041 \mu\text{m}$  for interference for a cell gap  $d = 3 \mu\text{m}$ , wavelength  $\lambda = 0.6 \mu\text{m}$ , and LC index of refraction  $n = 1.5$ . This agrees well with the observed peak-to-peak ripple spacing observed. Similarly, interference occurs with a change in cell gap,  $\Delta d = \lambda / (2n)$ , or  $0.2 \mu\text{m}$ . The variation in cell gap corresponds to a 6.9% change in cell gap, which implies a need for cell-gap control of better than 3.5%. When voltage is applied to produce an on state, the effective LC index of refraction changes from 1.5 to 1.6, resulting in both  $\Delta\lambda$  and  $\Delta d$  values that are 6% lower. Improved cell-gap control to within the above tolerances has eliminated the remaining 5% nonuniformity.

#### *Switching times*

The LC switching time is also important since, along with the SLM addressing and exposure times, it determines the SLM image-writing rate. The 45°-twisted-angle TN LC mode was found to have a 0%-90% or 100%-10% response time of about 20 ms at room temperature. At present, this LC speed is consistent with the requirements of the holographic storage media, but with need in the future for higher writing speed, faster LC modes will be required. The TN LC switching speed increases with rising temperature, and LC-response-limited frame rates up to 100 Hz at 50°C appear possible with the 54° TN mode.

While other nematic LCs with faster switching times have been reported [13, 14], the fastest LC switching times are achieved with ferroelectric liquid crystal (FLC) materials [15]. Surface-stabilized FLC materials have binary optical states and high contrast, and do not have twisted nematic disclination-like structures. However, the submicron gaps for FLC cells are very difficult to fabricate. FLC is also difficult to drive with an ordinary active-matrix array, since the cell capacitor must provide the polarization charge for complete switching. The requirement for an inverted or complementary image for charge compensation requires that the illumination be shuttered off during the image-reversal period, which reduces the effective page-writing rate by half. Since higher-recording-speed materials do not exist at this time, these issues have not been fully addressed.

### **Chip design**

The fabrication technology used for the one-megapixel SLM is identical to the reflective liquid crystal light-valve-array technology developed for projection displays [16]. Unlike gray-scale-display light-valve designs, the design of an SLM suitable for holographic data storage uses only bilevel information. This simplifies the integration of both row and column drivers with the array. The potential for contrast, efficiency, speed, and uniformity in the LC is constrained by silicon technology voltage limits and pixel size requirements.

The technology used for fabricating the SLM chip was based upon a 1.2- $\mu\text{m}$ , 5-V CMOS process modified for 10 V and two levels of polysilicon. A 10-V gate driver was needed to write 0-6-V pixel voltages. A modified 0.8- $\mu\text{m}$  process was incorporated for the second- and third-level metal. The second-level metal was dedicated to absorbing light passing through the spacing between mirrors. The third-level metal was dedicated for the mirrors. This left only one level of metal for general-purpose wiring. The thin-film patterning of the chip fabrication produces nearly 1  $\mu\text{m}$  of bow in the chip. Patterned

SiO<sub>2</sub> spacers were chosen for LC gap control for their strength and precise dimensional control. Design rules were also modified for 1x lithography, which allowed the fabrication of large chips.

The holographic spatial light-modulator chip consists of an active-matrix array, row drivers at both the left and right sides of the array, and column drivers. In conventional active-matrix addressing, the rows are selected one at a time from top to bottom of the array. The data presented on the column lines are written in the pixels of the selected row. As shown in **Figure 9**, the active-matrix pixel circuit is essentially a DRAM circuit. It consists of a single n-FET transistor whose gate is connected to a row line. The source is connected to a data line and the drain is connected to the mirror electrode. Approximately half of the drain-connected storage capacitance is formed by coupling the second level of polysilicon to a first polysilicon layer that functions as the previous row line. The cell storage capacitance was estimated to be about 75 fF. The cell size was minimized, given the process ground rules. The resulting cell pitch was 15.6  $\mu\text{m}$ . Both row- and column-driver circuits were designed to match that cell pitch.

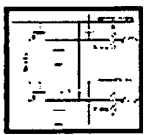


Figure 9

Row drivers drive both ends of each row to maximize the addressing rate using resistive polysilicon row lines. An improvement in line settling time by a factor of 4 is obtained by driving both ends. Redundancy was used in the row-selection data path. As shown in **Figure 10**, the row-driver circuit has four blocks of 256-row-selection circuitry. Each block has two groups of row-selection circuits. The inner group is used by default, but if it does not function, the outer group can be selected by grounding the appropriate input. The output of each group's row-selection data path is connected to an OR gate for signal propagation to the next block. One dynamic register is used for each row-selection circuit. The dynamic register consists of a complementary-clocked transmission gate for coupling data to an inverter. As shown in **Figure 11**, for odd-numbered rows, the inverter input is used for row-selection output, while for even rows, the inverter output is used. Use of the inverter input is possible if no other asynchronous transmission gates are connected. Out-of-phase clock signals to the odd and even dynamic registers are used to shift the row-selection data. This arrangement inherently provides for row-line precharging, since row-selection data exist in two adjacent circuits.



Figure 10



Figure 11

The row-line driver circuit consists of an ENABLE-signal clocked-OR level-shifting circuit, as shown in **Figure 12**. The dynamic circuit relies on a low-level ENABLE signal to reset the circuit by pulling up the input to the output inverter, thereby maintaining a low state on the row line. The high-level ENABLE state allows the row line to be driven high with a high row-selection input state. Edge control of two ENABLE signals, one for odd and one for even lines, allows control of row-line precharging and row-line turnoff.

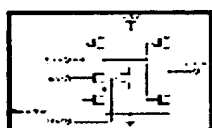
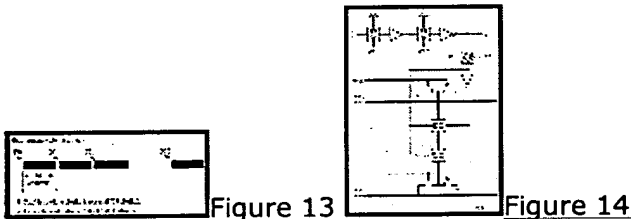


Figure 12

The function of the column driver is to connect one of four reference voltages to the

column line. Which reference is selected depends upon whether the data bit is logical 1 or 0 and whether the polarity input is 1 or 0. The overall organization of the row drivers is shown in **Figure 13**. Sixteen inputs provide data to sixteen 64-bit shift registers. Each bit in the 64-bit shift register provides data for an adjacent column line. The data-shifting direction is from left to right. To address 100 frames per second with data continuously supplied, a relatively low (6.5-MHz) clock rate is required. Two polarity-controlling inputs, each connecting only even- or odd-numbered columns, were incorporated to allow frame, row, column, or pixel inversion. **Figure 14** shows the data-driver circuit. The data shift register consists of two dynamic registers connected in series. Each dynamic register consists of a complementary transmission gate and an inverter. CK2 is the inversion of CK1. The data-loading register uses the same dynamic register design as that used in the data shift register. Both the input and the output of the inverter in the load register are used to drive transmission gates for the reference-selection circuitry. Two p-FET transistors are used for positive-reference selection, and the two n-FETs are used for negative-reference selection. If NPOL is high, the negative frame references are selected; otherwise, the positive frame references are selected. Two complementary transmission gates were used to connect the "on" (VN1 or VP1) or "off" (VP0 or VN0) reference to the data line.



Simulations of the row-driver circuits driving the polysilicon row lines gave a worst-case row rise and fall time of approximately 1  $\mu$ s. The 0%-90% rise time and 100%-10% fall time at the ends of the row lines were each less than 100 ns. However, the row-line skew time, the end-to-middle row-line transition time difference, was approximately 1  $\mu$ s. Data-driver simulations show that the 0-7-V, 0%-90% rise time was also 1  $\mu$ s. Using just the rise time as the time needed for the LC voltage would not deliver the full RMS voltage to the pixel. The data-driver circuit takes nearly 3  $\mu$ s to settle to within 10 mV, which would be sufficient for 4-bit gray-level operation. However, such accuracy may not be needed in a binary holographic storage application. An error of 100 mV corresponding to 2  $\mu$ s may be acceptable. The data driver was simulated with 20-MHz clock rates.

If not limited by data-driver shift rates, the sum of row-line skew (1  $\mu$ s) and data-line settling time (2  $\mu$ s) times the number of rows (1024) determines the minimum time (3.1 ms) required to address the array. The minimum address time provides a writing rate of about 300 frames per second using continuously clocked data at 20 MHz.

## Assembly and packaging

The LC cell process steps for the cover glass and silicon chip are, in sequence, inspection, cleaning, polyimide (PI) coating, PI pre-baking, PI final baking, buffing the PI films with a cotton cloth on a wheel, and cleaning. Peripheral sealant is then dispensed on the cover glass to form the surround for the LC cavity. The cover glass and the silicon chip are assembled into the LC cell with a bottom glass support for the silicon chip with a UV-curable glue between the support and the chip. Pressure is applied to the cover and bottom glass during curing. The cell gap is measured at the four corners and in the center by spectral interference [17]. The assembly is placed in a vacuum chamber for LC fill. The next step is the sealing of the injection hole with UV-curable glue. Afterward, cell-gap uniformity is checked using normally incident monochromatic light with a sheet polarizer placed on top of the cell and observing the fringes. One fringe corresponds to a variation in cell gap of about 0.2  $\mu$ m. Finally, the cell is tested as a function of applied

voltage in which the reflected polarization conversion is measured with a photodiode.

The packaging of the SLM involves integrating the assembled liquid crystal cell onto an electronic card having a connector that is used for communication between an interface card and the SLM. The SLM is housed on an aluminum base assembly and anchored in place with a low-temperature-curing epoxy. This subassembly is attached to the card with four screws that have adequate clearance to permit the relative positioning of the card with respect to the SLM so that the wire-bonding pads on the two parts are aligned. The screws are then tightened to hold the pieces in alignment. The electrical connection between the silicon chip and the card is accomplished by wire bonding directly from the aluminum pads on the chip to gold-coated wire-bond pads on the card. This is the first example of a simplified light-valve or SLM package in which the SLM is directly connected to the gold-coated pads on the circuit board, eliminating the need for an intermediate flex circuit. **Figure 15** is a photograph of the packaged assembly. A black anodized aluminum frame and base plate serve not only to mechanically attach the SLM to the card but as a means to mount and align the SLM in an optical system.

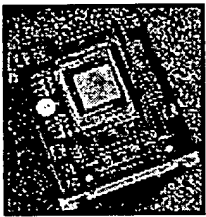


Figure 15

## Data control and interface electronics

As shown in **Figure 16**, the approach for supplying data uses two computers; a remote-user-interface computer is connected by an RS-232 interface to a host PCI bus computer with an SXGA graphics display adapter having both digital and analog outputs. A laptop running Visual Basic graphical user interface programs under Windows\*\* 3.1, 95, or NT was used as the remote computer. The display adapter software on the host computer runs from DOS and requires no other operating system. A host program was written to map or translate an SLM image into the frame-buffer image in the display adapter. This allows data to be written correctly to the SLM. The two-step process required that the proper 16 bits for the SLM data-driver inputs be extracted from the 1024 x 1024 x 1 SLM data image and positioned properly in the 1280 x 1024 x 24-bit frame buffer for transfer. **Figure 17** shows that the left-to-right shift direction of the SLM column-driver data requires the data to be reversed in the frame buffer, since the frame-buffer contents are output in raster fashion from left to right. The 16 bits of SLM input data are remapped as a single 24-bit frame-buffer pixel. **Figure 18** illustrates that the SLM frame-buffer pixel data for one SLM row are separated every 20 frame-buffer pixels across the frame-buffer row. Reduction in the data separation has allowed encoding three and four SLM lines into a single frame-buffer line.

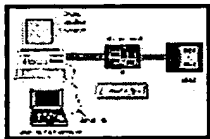


Figure 16

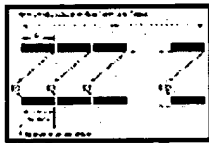


Figure 17

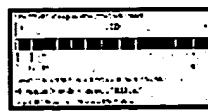


Figure 18

As shown in **Figure 19**, the digital output of the graphics card supplies dual, adjacent-color pixel data at 55 MHz. Only the even-pixel data outputs are used to provide data to the SLM. Each pixel output contains 24 bits of data; 16 are assigned as SLM data bits, two bits are used for the data-valid signal (providing clock edges for the SLM data) and SLM vertical sync, and the rest are unused. Two bits from the odd-pixel outputs are used for SLM horizontal sync and blanking. The third bit is optional and is used for low- and high-speed addressing rates. Shown in **Figure 20** is the method used to provide



two SLM data and timing-signal frames in the frame buffer. Each frame-buffer row provides three rows of SLM data. The SLM horizontal synchronizing signal (H) precedes each SLM data row, the SLM blanking signal (B) appears at the end of the frame buffer, and the SLM vertical sync signal is a full frame-buffer row preceding each frame of SLM data.

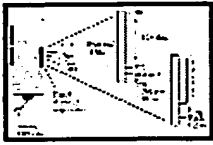


Figure 19

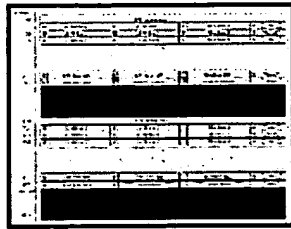


Figure 20

An interface card between the display adapter and the SLM is needed to convert the SLM horizontal, vertical, and blanking signals into row-selection data, row-clock, row-enable, data-clock, data-load, and frame-polarity signals. This is accomplished using a field-programmable gate array. A shutdown feature is provided to protect for over and under +5-V and +10-V input power. The interface card also contains the four reference voltages for the data drivers.

The remote-host graphical user interface consists of three screens. The first is the SLM User Interface, which is used to translate different image data types into a frame-buffer SLM data image. The second and most useful interface is the SLM Data Selection Panel, as shown in **Figure 21**. Most of the data-selection options were used for testing the SLM system. The user \*.SLM and \*.BIN options allow the user to specify lists of image files to be displayed. A third user interface panel is the SLM Pixel Write Utility for manually writing any arbitrary pixel data pattern anywhere in the 1024 x 1024 array, pixel by pixel.

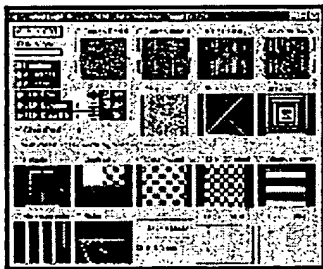


Figure 21

The data translation software, graphical user interfaces, and an SLM interface card allow dynamic SLM verification with arbitrary images. With two SLM frames loaded into the frame buffer, an update of five different images per second has been demonstrated using a 90-MHz Pentium computer. With one SLM image loaded into the frame buffer, rates of 12 different images per second have been demonstrated. The rate is higher, since less information is written to the display adapter. However, since the frame-buffer writing process is asynchronous and does not take exactly an even number of frames, LC charge imbalance could occur. To avoid this, a 50% on/off-pixel data requirement over some predetermined number of images would have to be encoded. This restriction can be circumvented by encoding two (one positive- and one negative-polarity) SLM frames into the frame buffer and updating both positive- and negative-polarity SLM pixel data simultaneously. Finally, three SLM frames were loaded into the frame buffer and were used to determine whether the SLM would function properly with a 180-Hz frame addressing rate and a 28-MHz data clock. If data could be provided continuously, the 28-MHz clock rate would correspond to an addressing rate of 430 frames per second. At this rate, nearly perfect images were obtained, but data chatter and data-driver block boundaries were observed.

This system is not limited to just encoding three SLM frames into the frame buffer. The SLM interface card can be modified to allow the odd-pixel spaces in the adapter to be used for SLM data. If the data-valid signal edges were used, SLM data could be positioned on adjacent frame-buffer pixel positions. This would allow up to 12 SLM frames to be written for each frame image. The 12 SLM frames could comprise six separate images for a burst writing rate of 240 pages per second. However, the average page-writing rate is limited by being able to write only one byte at a time to the frame buffer and associated adapter card, and also by PC system clock rates.

## CCD imaging test results

To test the suitability of the SLMs for holographic data storage, two SLM assemblies were viewed under conditions similar to those of a holographic storage system with a pixel-matched CCD camera. The collimated beam from an argon-ion laser (514 nm) illuminated the SLMs through a polarizing beam-splitting cube, which served as both polarizer and analyzer, and the light transmitted through the analyzer was imaged onto a CCD camera with 1536 x 1024 pixels, a 100% pixel fill factor, and 16-bit gray-scale resolution. Because the pixel pitch of the CCD (9  $\mu\text{m}$ ) did not match that of the SLM, a commercial photographic macro lens ( $f = 60$  mm, aperture  $f/2.8$ ) was used to demagnify the SLM image by a factor of 15.6/9, so that each SLM pixel was imaged onto one CCD pixel. In principle, this approach allows the inspection of the entire SLM in one operation. By applying various test patterns, it is possible to characterize response uniformity and contrast at all spatial frequencies. In this experiment, the use of an off-the-shelf objective lens limited the performance of the test system: The observed uniformity and point-spread function were degraded because of vignetting in the lens and uncompensated spherical aberration introduced by the beam-splitting cube. Also, the optical magnification was adjusted to an accuracy of only about 0.05%, or one quarter of a pixel. With custom optics and careful optomechanical design, it is possible to achieve considerably more accurate pixel matching and more uniform illumination [18]. Hence, these measurements represent a lower limit for the performance of which the SLM is capable.

Despite the limitations of the optics, it was possible to show that the performance of the SLMs at high spatial frequencies was adequate to encode binary data for holographic storage. To minimize the impact of the imperfections in the viewing optics, and to avoid a few defective pixels on the SLMs, data patterns were programmed in a 512 x 512-pixel region at the center of the SLMs. This represents an error of about one tenth of a pixel, assuming perfect alignment of the SLM pixels to the CCD pixels. Restricting the measurements to a 512 x 512-pixel region in this test setup is representative of an actual recording system having registration to one tenth of a pixel. **Figure 22** shows the response of the CCD camera to a data pattern encoded using a balanced modulation code [19] and a Reed-Solomon error-correcting code. Comparable results were obtained for both of the tested SLMs. Ideally, the CCD pixels viewing "on" SLM pixels (closed circles) would see a uniformly high light level, while those viewing "off" SLM pixels (open circles) would see a uniformly low light level. In reality, finite SLM contrast, optical imperfections, misalignment, and diffraction all act to broaden the ideal response. Where the on and off distributions overlap, the input data cannot be reconstructed on the basis of CCD response alone; this applies to 0.8% of the pixels in **Figure 22**. However, by using the information in the modulation and error-correcting codes, the original data could be recovered without any errors.

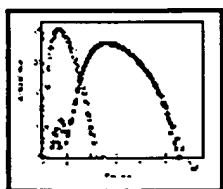


Figure 22

## Concluding remarks

A one-megapixel SLM specifically designed for the holographic storage application has been designed and built. The writing capability of the reflective SLM produced bit-error-free CCD images using error-correction and modulation codes. Special antireflection coatings and cell-gap control of better than 0.1  $\mu\text{m}$  are needed to minimize interference using coherent monochromatic illumination. Adequate (4:1) resolution-limited contrast has been achieved by using frame inversion and minimizing the on-to-off-state voltage difference. While the 54° TN LC response speed is only about 20 ms, present holographic material recording rates are even slower. Data were clocked into the SLM at an equivalent rate of 300 frames per second. A system providing SLM data using a display adapter and an interface card was used to write arbitrary data to the SLM. SLM page-writing rates of up to 12 pages per second were demonstrated, which is also about the maximum page-writing rate for iron-doped  $\text{LiNbO}_3$ .

## Acknowledgments

Several individuals helped make the one-megapixel SLM system possible: Jagat Mavani, Steven Kosonocky, and Arthur Bright helped with chip design and layout. Steven Lovas, Harold Ifill, Ray Horton, and Keith Fogel provided assistance with the SLM packaging design and assembly. Evan Colgan arranged and operated the confocal microscope, and Ken Ho helped with the scattered- light confocal microscope image manipulation.

This research was performed as part of the Holographic Data Storage System (HDSS) consortium for the National Storage Industry Consortium. We wish to thank the other members of the HDSS consortium for numerous technical discussions and the Defense Advanced Research Projects Agency for financial support under Contract No. MDA-972-95-3-0004.

## References

*Received March 17, 1997; accepted for publication March 16, 1998*

---

[ [Journals home page](#) | [Subscribe/order](#) | [Current issue](#) | [Recent issues](#) | [Description](#) ]

[IBM Home](#) | [Shop](#) | [Contact IBM](#) | [Search](#) | [Privacy](#) | [Legal](#)

©1998 IBM Corporation